

REPORT DOCUMENTATION PAGE

Form Approved
OMB No. 0704-0188

The public reporting burden for this collection of information is estimated to average 1 hour per response, including the time for reviewing instructions, searching existing data sources, gathering and maintaining the data needed, and completing and reviewing the collection of information. Send comments regarding this burden estimate or any other aspect of this collection of information, including suggestions for reducing the burden, to Department of Defense, Washington Headquarters Services, Directorate for Information Operations and Reports (0704-0188), 1215 Jefferson Davis Highway, Suite 1204, Arlington, VA 22202-4302. Respondents should be aware that notwithstanding any other provision of law, no person shall be subject to any penalty for failing to comply with a collection of information if it does not display a currently valid OMB control number.

PLEASE DO NOT RETURN YOUR FORM TO THE ABOVE ADDRESS.

1. REPORT DATE (DD-MM-YYYY) 24072206			2. REPORT TYPE Final Report		3. DATES COVERED (From - To) 1 February 2003 - 31 December 2005	
4. TITLE AND SUBTITLE Model-Based Feedback Control of Cavity Resonance: An Experimental and Computational Approach				5a. CONTRACT NUMBER		
				5b. GRANT NUMBER F49620-03-1-0074		
				5c. PROGRAM ELEMENT NUMBER		
6. AUTHOR(S) Professor David Williams				5d. PROJECT NUMBER		
				5e. TASK NUMBER		
				5f. WORK UNIT NUMBER		
7. PERFORMING ORGANIZATION NAME(S) AND ADDRESS(ES) Mechanical & Aerospace Engineering Illinois Institute of Technology 3110 South State Street Chicago IL 60616				8. PERFORMING ORGANIZATION REPORT NUMBER		
9. SPONSORING/MONITORING AGENCY NAME(S) AND ADDRESS(ES) USAF/AFRL AFOSR 875 North Randolph Street Arlington VA 22203 <i>Dr John Schmusseur/NA</i>				10. SPONSOR/MONITOR'S ACRONYM(S) AFOSR		
				11. SPONSOR/MONITOR'S REPORT NUMBER(S)		
12. DISTRIBUTION/AVAILABILITY STATEMENT Distribution Statement A. Approved for public release; distribution is unlimited. AFRL-SR-AR-TR-06-0387						
13. SUPPLEMENTARY NOTES						
14. ABSTRACT This report presents results of experiments and numerical simulations studying closed-loop feedback control of oscillations in the compressible flow past a rectangular cavity. When weapons bays are exposed to high flow speeds, extremely large pressure fluctuations result, and are often large enough to cause structural damage to the aircraft and internal stores. The goal of this work is to design an implement a model-based feedback controller to suppress oscillations in the flow past a cavity over a range of operating conditions, using much less power than open-loop techniques; and to understand the physics well enough to allow the techniques to be reliably transferred to full-scale aircraft. Several specific advances have been made in this work, relevant for cavity flow control as well as for other closed-loop flow control applications. Theoretical models are presented for temporally developing shear layers and cavity oscillations at the flow conditions used in both simulations and experiments. These models can be used to construct dynamic observers, which reconstruct the full flow information from a limited number of sensors, and significantly outperform static estimators such as Linear Stochastic Estimation (LSE).						
15. SUBJECT TERMS						
16. SECURITY CLASSIFICATION OF:			17. LIMITATION OF ABSTRACT UU	18. NUMBER OF PAGES 58	19a. NAME OF RESPONSIBLE PERSON	
a. REPORT UU	b. ABSTRACT UU	c. THIS PAGE UU			19b. TELEPHONE NUMBER (Include area code)	

Best Available Copy

Standard Form 298 (Rev. 8/98)
Prescribed by ANSI Std. Z39.18

Model-Based Feedback Control of Cavity Resonance: An Experimental and Computational Approach

Clarence W. Rowley David R. Williams

AFOSR Grant numbers F49620-03-1-0081 and F49620-03-1-0074

24 July 2006

Abstract

This report presents results of experiments and numerical simulations studying closed-loop feedback control of oscillations in the compressible flow past a rectangular cavity. When weapons bays are exposed to high flow speeds, extremely large pressure fluctuations result, and are often large enough to cause structural damage to the aircraft and internal stores. The goal of this work is to design and implement a model-based feedback controller to suppress oscillations in the flow past a cavity over a range of operating conditions, using much less power than open-loop techniques; and to understand the physics well enough to allow the techniques to be reliably transferred to full-scale aircraft.

Several specific advances have been made in this work, relevant for cavity flow control as well as for other closed-loop flow control applications. Theoretical models are presented for temporally developing shear layers and cavity oscillations at the flow conditions used in both simulations and experiments. These models can be used to construct dynamic observers, which reconstruct the full flow information from a limited number of sensors, and significantly outperform static estimators such as Linear Stochastic Estimation (LSE). The models can also be used to design feedback controllers, and a model-based controller was shown to completely eliminate oscillations in fully resolved 2D direct numerical simulations. Suppression of cavity oscillations by closed-loop control has been demonstrated in simulations, as well as both subsonic and supersonic experiments, with good agreement with model predictions.

Contents

1	Introduction	2
1.1	Aerospace interest	3
1.2	Goals	4
1.3	Challenges and limitations	5
1.4	Outline of this report	6

20061016133

2	Shear layer modeling	8
2.1	Introduction	8
2.2	Direct numerical simulations	9
2.3	Low-dimensional models	10
2.3.1	Scaling basis functions	10
2.3.2	Equations of motion for the thickness	11
2.3.3	Projection of flow equations	12
2.4	Results	14
2.4.1	Flow with mode $k = 1$ only	14
2.4.2	Flow with both modes $k = 1$ and $k = 2$	17
2.5	Summary and future work	22
3	Subsonic cavity experiments	23
3.1	Experimental setup	23
3.2	Results	26
3.2.1	Cavity response to open-loop and closed-loop forcing	26
3.2.2	System identification and linear models	28
3.3	Summary	31
4	Supersonic cavity experiments	32
4.1	Experimental setup	33
4.2	Results	36
4.2.1	Baseline cavity behavior - no forcing	36
4.2.2	Cavity response to periodic forcing	38
4.2.3	Closed-loop cavity response	41
5	Subsonic numerical simulations	42
5.1	Empirical Galerkin models	43
5.1.1	Dynamic observers	45
5.1.2	Model-based control design	45
5.2	Dynamic phasor models	47
5.2.1	Controller design	47
5.2.2	Observer design	48
5.3	Results	49
5.3.1	Comparison of dynamic and static observers	49
5.3.2	Closed-loop control in full simulations	50
5.4	Summary	53
A	Equations and coefficients in the two-mode shear layer model	53

1 Introduction

Flow over the simple geometry of a cavity produces a rich variety of flow phenomena including resonant tones, multiple flow and acoustic instabilities, and complex wave



Figure 1: Schlieren image cavity flow at $M = 0.4$, $L/D = 2$, from [17].

interactions. Although the cavity flow is a complicated dynamical system, it is comprised of only four elemental fluid dynamic processes: shear layer amplification of vortical disturbances, pressure wave generation through vortex-surface interaction, upstream propagation of acoustic waves, and receptivity at the upstream edge of the cavity, converting pressure waves into vorticity waves. In Fig. 1, a schlieren image obtained by Kegerise[17] shows three coherent vortices in the shear layer over a resonant cavity at $M = 0.4$. Motivated by the need to suppress the large amplitude resonant tones that can quickly lead to structural damage in aircraft, understanding and controlling the flow over cavities has been of interest in the aerospace field since the 1950s [20].

The cavity problem is a challenge to our ability to control complex flow systems. While the solution seems simple enough—any scheme that disrupts the resonance mechanism can be used to suppress resonant tones—experience has shown that finding a practical solution is not trivial. Passive, active open-loop and closed-loop control architectures all have serious limitations. Passive techniques generally do not work over a wide range of flow speeds, and extract large amounts of energy from the mean flow in the form of increased drag. Active open-loop methods are often limited by actuator bandwidth or require large actuator power to be effective. Prior to this report closed-loop control techniques have not been demonstrated above Mach number $M = 0.74$ [6] and introduce greater complexity. Cattafesta, et al.[4] provide an extensive review of cavity flow control techniques. Their classification scheme for active flow control is shown in Fig. 2, and is adopted for this report.

It is important to understand that passive and active open-loop control schemes break the cycle of resonance in a fundamentally different manner than closed-loop approaches. Because the dynamics of a linear system cannot be changed with open-loop control, any open-loop actuator modifying the cavity resonance must do so at finite amplitudes, typically at amplitudes comparable to the tones being suppressed. By contrast, closed-loop control acts by changing the dynamics of the linear system, which implies low-power actuators can be used effectively.

1.1 Aerospace interest

Cavity flows arise in many aerospace applications, such as wheel wells, weapons bays, and other fuselage openings for telescopes and sensors. Resonant tones can reach 170 dB sound pressure level [9], corresponding to r.m.s. pressure amplitudes

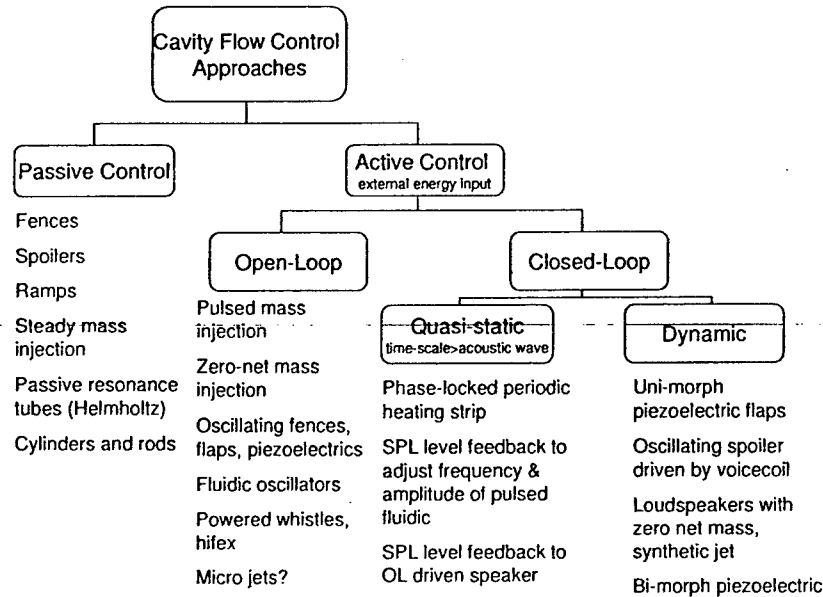


Figure 2: Classification of flow control schemes, from [4].

of 6,300 Pa (0.92 psi). Not only are the amplitudes large, but the pressure waves are also spatially correlated, which quickly leads to structural fatigue issues inside the aircraft. In addition to the sound pressure levels of individual tones, the broadband spectrum can also be of concern in practical applications, and overall sound pressure level (OASPL) is often used as a metric for comparisons.

Control of acoustic tones is closely coupled with flight vehicle drag and store separation characteristics. The aerodynamic drag on cavities was measured by [21] to be 250% higher during acoustic resonance than under non-resonant conditions. Deployable fences at the upstream end of the cavity are commonly used on aircraft to modify the shear layer development. In addition to suppressing acoustic tones, fences also modify the internal mean flow in the cavity, providing favorable store separation characteristics. These are important effects to be considered in the design of practical flow control systems.

1.2 Goals

Ideally the research on active flow control for cavities will lead to practical applications. Key goals for all control architectures are to suppress the acoustic tones to background sound pressure levels, over a range of flight conditions, with the smallest possible actuator requirements, resulting in reduced drag and possibly enhanced store separation characteristics.

Closed-loop control systems will only buy their way onto aircraft after demon-

strating performance benefits that exceed the additional cost and complexity relative to passive and open-loop controllers. The anticipated benefits in performance from closed-loop control address many of these goals, most importantly low power, and adaptability to changing flight conditions.

More academic goals also exist. The cavity problem is an ideal test case for exploring and evaluating flow control architectures and algorithms. Simple passive, open-loop and closed-loop control architectures suppress tones by different physical mechanisms. Modern dynamical systems and control theory can be used to design better control systems, and the theory can be tested by the response of the cavity flow. For example, a simple analog feedback controller with gain and time delay will suppress resonant tones by about 18 dB to 20 dB. Attempts to achieve additional noise suppression by increasing the gain of the feedback signal often fail, sometimes due to fundamental limitations of any controller. More general goals are therefore to develop methodologies for designing effective controllers for complex flow systems from first principles; understand any fundamental limitations for a given configuration of sensors and actuators; predict actuator requirements (e.g., bandwidth and power); and optimize the number and placement of sensors and actuators.

To achieve these goals it is necessary to have some understanding of both the control theory and the cavity flow physics. With an appropriate model of the overall system, one can predict the achievable limits of sound suppression, and determine actuator bandwidth and sensor requirements. Such knowledge is essential to the design of control systems for applications. It reduces the need for trial and error, and prevents attempts at achieving the impossible.

1.3 Challenges and limitations

There are several hurdles to clear before active flow control will be used on modern aircraft for cavity tone control. First, suitable actuators must be developed. Actuators for closed-loop control do not have sufficient bandwidth or amplitude to operate effectively over a wide range of flight conditions. Some open-loop control actuators have been successful at higher subsonic and even supersonic Mach numbers, but these have large power requirements.

Second, one needs to know the appropriate relations to scale the actuators from the laboratory to flight conditions. Dynamic pressure and various cavity dimensions have been used to scale data, but there is no consensus on the correct parameters.

Next, some understanding of the response of the cavity to open-loop forcing is needed. It is somewhat surprising, given the large number of cavity control studies, that the response of the cavity to open-loop forcing is still not well understood. At this time, we are aware of no model that predicts this response. Open-loop response of a supersonic cavity is discussed.

Finally, in the case of closed-loop control, efficient and robust control algorithms are needed to insure that control is maintained when flight conditions change.

Much of the recent experimental and theoretical work on control of cavity oscillations has focused on compressible flow, largely because of aerospace applications. Several review articles describe and classify cavity flows in different regimes: in par-

ticular, [28, 29] classify oscillation regimes as *fluid dynamic*, in which shear layer dynamics play a role, and *fluid resonant*, in which shear layer dynamics are secondary, and the acoustics are important. Our emphasis is on the fluid dynamic regime, which occurs in shallow cavities at Mach numbers of interest to most aerospace applications (high subsonic and low supersonic). The fluid resonant regime is relevant for Helmholtz resonators and automobile sunroofs [19, 18], and detailed models of the dynamics at very low Mach numbers have been studied by [16], but we focus on compressible flows ($M > 0.2$) extending into the supersonic regime. An overview of much of the recent work is given in our review article [35]. The recent reviews of [8] and [4] are other excellent references for the flow regimes we examine here.

1.4 Outline of this report

The main contributions of this report are as follows. Section 2 discusses theoretical models of a temporally growing free shear layer, in order to better understand the fundamental mechanisms governing energy transfer between modes in a shear layer, and how these affect the overall spreading rate of the shear layer. These results have been published in [55], and the main results are as follows:

1. Low-dimensional models were obtained that describe the growth, decay, and interaction of Kelvin-Helmholtz modes, by scaling the y coordinate dynamically as the shear layer spreads in time.
2. The models have the form of nonlinear oscillators, coupled to a differential equation for the shear layer thickness.
3. The resulting models capture growth, saturation, pairing (energy transfer between modes), and how each of these effects couples to the spreading rate of the shear layer.
4. This work provides a groundwork upon which more complicated models may be built, describing spatial evolution, and the effects of forcing on energy transfer and spreading rate.

Section 3 discusses experiments on a subsonic cavity flow, conducted at the Gas Dynamics Laboratory at Princeton University, over a Mach number range 0–0.67. Much of this work has been published in [57], and the main results are as follows:

1. Rossiter mode lock-on was shown to be the effect of an acoustically hard ceiling. Spurious wind-tunnel modes were suppressed using an open-celled acoustic foam, and after this modification the measured frequencies of oscillation matched those predicted by the Rossiter formula, without lock-on.
2. The response of a zero-net-mass actuator agreed with predicted response using an exponential horn equation, and the actuator maintained authority up to $M = 0.55$.

3. The presence of large-amplitude oscillations does not imply the oscillations are self-sustained: for most (possibly all) of the flow conditions studied here, the cavity flow behaves as a stable amplifier with sharp resonant peaks, that amplifies disturbances preferentially at the resonant frequencies. Oscillations are sustained by the constant presence of external disturbances, such as boundary layer turbulence.
4. Closed-loop control was able to suppress cavity tones by 12dB at a Mach number $M = 0.45$.
5. Linear models produce good qualitative agreement with the experimental results.

Section 4 presents the results of supersonic cavity experiments conducted in a wind tunnel at Illinois Institute of Technology, at $M = 1.86$. Some of this work is to appear in [56], and the main results and conclusions are as follows:

1. Open-loop forcing was used to document linear behavior of Rossiter modes in a supersonic cavity.
2. Closed-loop control of the 2nd Rossiter mode was demonstrated at $M = 1.86$
3. Overall Sound Pressure Level (SPL) scales linearly with stagnation pressure (equivalent to dynamic pressure) in a supersonic flow

Finally, Section 5 presents the results of models and controllers developed from numerical simulations. These have been published in [32], and the main results are as follows:

1. Low-dimensional models were obtained using Proper Orthogonal Decomposition (POD) and Galerkin projection.
2. These models were used to develop *dynamic* observers, to reconstruct the entire flow state from a single sensor, and the resulting observers dramatically outperform static estimators such as Linear Stochastic Estimation (LSE).
3. The effect of actuation was incorporated into the POD models, as well as into a phenomenological model, a simple nonlinear oscillator.
4. Optimal controllers designed naively from the POD/Galerkin model control the model well, but fail on full simulations, as the controlled flow leaves the region of validity of the model.
5. Controllers designed to respect the region of validity of the model stabilize the full simulations, and the model predictions closely match results from the full simulations.
6. A controller designed as above stabilizes oscillations in the full simulation, using a zero-net-mass actuator at the leading edge of the cavity, and a single wall pressure sensor. In the absence of noise, oscillations are completely eliminated.

2 Shear layer modeling

In this section, we develop low-dimensional models for the evolution of a free shear layer in a periodic domain. The goal is to obtain models simple enough to be analyzed using standard tools from dynamical systems theory, yet including enough of the physics to model nonlinear saturation and energy transfer between modes (e.g., pairing). Recently, experiments have suggested that high-frequency forcing of shear layers over open cavities may provide a mechanism for suppression of tones in cavities, and a long-term goal of this work is to study the dynamics of forced shear layers, to better understand these effects.

In the present work, 2D direct numerical simulations of a spatially periodic, temporally developing shear layer are performed. Low-dimensional models for these dynamics are obtained using a modified version of proper orthogonal decomposition/Galerkin projection, in which the basis functions can scale in space as the shear layer spreads. Equations are obtained for the rate of change of the shear layer thickness. When scaling is included in the shear flow dominated by $k = 1$ only, the first POD mode of wave number $k = 1$ captures 93% of the energy, which is impossible to obtain by regular POD analysis without scaling. For the flow dominated by both $k = 1$ and $k = 2$, when scaling is included, the first POD mode of wave number $k = 1$ and $k = 2$ together capture 95% of the total energy. Projection of incompressible Navier-Stokes equations to the first two POD modes of $k = 1$ gives a simple 2-mode model. If the projection is onto the first two POD modes of both $k = 1$ and $k = 2$, a more complex 4-mode model can be built to describe more complex flows. The 2-mode model can describe certain single-frequency features of the system, such as vortex roll-up, nonlinear saturation, and viscous damping. The 4-mode model can describe interactions between two frequencies (vortex merging) as well. The relation between the phase difference of the first (symmetric) and second (asymmetric) POD modes of the same wave number and the shear layer spreading rate can be clearly observed in both direct numerical simulations and model computations.

The work described in this section has been published as an AIAA conference paper in [55].

2.1 Introduction

Temporally and spatially evolving shear layers have been studied for over a century, dating back to the early experiments of Helmholtz and Lord Kelvin, and the analysis of Lord Rayleigh, which laid the foundations for stability analysis we still use today[10, 41]. This paper focuses on nonlinear models for the evolution in time of a spatially periodic shear layer, including nonlinear effects such as saturation of disturbances and energy transfer between modes.

The motivation comes primarily from the study of oscillations in the flow past a cavity, in which recent experiments suggest that periodic forcing of the shear layer may reduce or eliminate the resonant tones produced for the unforced flow[46]. The mechanisms for these effects are not understood, and indeed there is some question about whether the experimentally observed suppression of oscillations re-

sults from the high-frequency effects or from modifications to the mean flow. However, simple mechanical systems often exhibit striking changes in dynamical features when subjected to high-frequency forcing, and given an appropriate (relatively low-dimensional) model, these effects can often be analyzed and understood using techniques from dynamical systems theory (e.g., averaging)[14, 51]. The eventual goal of this work is to produce such nonlinear models of shear layer dynamics, suitable for analysis, in order to better understand mechanisms of pairing, saturation, and cavity tone suppression.

The general technique we use is based on Proper Orthogonal Decomposition (POD) and Galerkin projection, but differs from the standard technique, in that we use basis functions that are able to change their spatial scale as the shear layer thickness changes. A related technique has been used in previous works, for traveling solutions and self-similar solutions[34, 33]. In this method, empirical basis functions are computed from numerical data that is first scaled so that it matches up best with a preselected “template”. Often models of much lower dimension are possible in such a scaled reference frame.

We describe the simulations in section 2.2, the low-dimensional modeling procedure in section 2.3, and finally present the results in section 2.4.

2.2 Direct numerical simulations

The flow considered here is a two-dimensional free shear layer periodic along the streamwise (x) direction, as shown in figure 3. The compressible Navier-Stokes equations are solved in a domain $0 < x/\delta_{\omega 0} < 5\pi$ and $-30 < y/\delta_{\omega 0} < 30$, where $\delta_{\omega 0}$ is the initial vorticity thickness. A spectral method was naturally chosen for x -direction derivatives, and fourth-order dispersion-relation-preserving scheme [50] was used for derivatives along the y direction. A fourth-order Runge-Kutta algorithm was used to advance the solution in time. In the simulation, an additional $20\delta_{\omega 0}$ thickness buffer zone was attached to the top and the bottom of the above domain to enhance the non-reflecting boundary conditions [12].

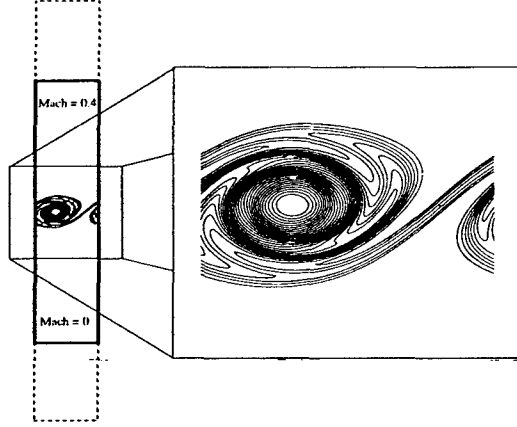


Figure 3: Schematic of the two-dimensional free shear layer simulation.

The flow was started with a hyperbolic tangent velocity profile $u_0(x, y) = U_\infty(1 + \tanh(2y))/2$ with small perturbations, which are eigenfunctions of the most unstable modes (for streamwise wave number $k = 1$ or $k = 2$ in different cases) calculated from the linear stability analysis.

2.3 Low-dimensional models

2.3.1 Scaling basis functions

A common approach to low-dimensional modeling is to project the governing equations onto a fixed set of basis functions, which are often determined by proper orthogonal decomposition of a set of data. Here, since the shear layer thickness is spreading in time, because of vortex rolling up, vortex merging, Reynolds stresses, and viscous dissipation, we consider basis functions that scale in the y -direction. In particular, denoting the vector of flow variables by $q = (u, v)$ (only the velocity field is considered for now), we expand

$$q(x, y, t) = r(x, g(t)y, t) \quad (1)$$

where $g(t) > 0$ is a scaling factor, and

$$r(x, y, t) = \varphi_0(y) + \sum_{j=1}^n a_j(t) \varphi_j(x, y), \quad (2)$$

where $\varphi_0(y)$ is typically the mean flow, and φ_j are basis functions (typically found by POD). The choice of the scaling factor $g(t)$ is arbitrary, but following the approach in previous works[34, 33], here we choose it so that $r(x, y, t)$ lines up best with a pre-selected *template function* $r_0(x, y)$, which here might be a parallel tanh profile (e.g., $r_0(x, y) = U_\infty(1 + \tanh(2y))/2$). With this definition of $g(t)$, a new thickness can be defined as

$$\delta_g = \delta_{\omega 0}/g(t) \quad (3)$$

It is not surprising that this “ g ” thickness is very close to vorticity thickness in our flow. The condition that r be scaled so that it most closely matches r_0 may be written

$$\left. \frac{d}{ds} \right|_{s=0} \|r(x, y, t) - r_0(x, h(s)y)\|^2 = 0,$$

where $h(s)$ is any curve in \mathbb{R}^+ with $h(0) = 1$, and $\|\cdot\|$ is a norm on the space of functions of (x, y) : that is, $h = 1$ is a local minimum of the error norm above. This expression becomes

$$-2 \left\langle \left. \frac{d}{ds} \right|_{s=0} r_0(x, h(s)y), r(x, y, t) - r_0(x, y) \right\rangle = 0$$

which becomes

$$\left\langle y \frac{\partial r_0}{\partial y}, r - r_0 \right\rangle = 0. \quad (4)$$

Geometrically, this result means that the set of all such functions r that are scaled so that they most closely match the template r_0 is an affine space through r_0 and orthogonal to $y \partial_y r_0$.

2.3.2 Equations of motion for the thickness

Here, we obtain equations of motion for the rate of change of the parameter $g(t)$, which governs the shear layer thickness. We regard the equations of motion as a dynamical system evolving on a function space H , consisting of the flow variables at all points (x, y) in our spatial domain. Thus, $q(t) \in H$ is a snapshot of the entire flow at time t , and the governing equations of motion may be written

$$\partial_t q(t) = f(q(t)), \quad (5)$$

where f is a differential operator on H (e.g., the Euler or Navier-Stokes equations). If we introduce the scaling operator $S_g : H \rightarrow H$, defined by

$$S_g[q](x, y) = q(x, gy), \quad \forall g \in \mathbb{R}^+$$

then the expansion (1) becomes $q(t) = S_g[r(t)]$, and the governing equations may be written

$$\frac{\partial}{\partial t} S_{g(t)}[r(t)] = f(S_{g(t)}[r(t)]).$$

Since

$$\begin{aligned} \frac{\partial}{\partial t} S_{g(t)}[r(t)](x, y) &= \frac{\partial}{\partial t} r(x, g(t)y, t) \\ &= \frac{\partial r}{\partial t}(x, gy, t) + \dot{g}y \frac{\partial r}{\partial y}(x, gy, t) \\ &= S_g \left[\frac{\partial r}{\partial t} \right](x, y) + \frac{\dot{g}}{g} S_g \left[y \frac{\partial r}{\partial y} \right](x, y), \end{aligned}$$

the equations of motion become

$$S_g \left[\frac{\partial r}{\partial t} \right] = f(S_g[r]) - \frac{\dot{g}}{g} S_g \left[y \frac{\partial r}{\partial y} \right]. \quad (6)$$

If we define $f_g(r) = S_{1/g}f(S_g[r])$, then these may be written

$$\frac{\partial r}{\partial t} = f_g(r) - \frac{\dot{g}}{g}y \frac{\partial r}{\partial y}. \quad (7)$$

Thus, the equations for the evolution of the scaled variable r in (1) are similar to the original dynamics (5), with f replaced by f_g , and with one additional term related to the rate of change of the scaling factor $g(t)$. These equations alone are not enough to specify the evolution $r(t)$, though, since we also need to specify the scaling $g(t)$. However, when (7) is solved along with the constraint (4), then this forms a partial differential algebraic equation which completely specifies both r and g . Differentiating the constraint (4), we have

$$\begin{aligned} \left\langle y \frac{\partial r_0}{\partial y}, \frac{\partial r}{\partial t} \right\rangle &= 0 \\ \Rightarrow \left\langle y \frac{\partial r_0}{\partial y}, f_g(r) - \frac{\dot{g}}{g}y \frac{\partial r}{\partial y} \right\rangle &= 0, \end{aligned}$$

which becomes

$$\frac{\dot{g}}{g} = \frac{\langle f_g(r), y \partial_y r_0 \rangle}{\langle y \partial_y r, y \partial_y r_0 \rangle}. \quad (8)$$

Altogether, equation (7) for r together with equation (8) for g completely specify the evolution, and substituting the expansion (2) and taking inner products with φ_k determines low-dimensional models in terms of the coefficients $a_k(t)$ and the scaling $g(t)$.

2.3.3 Projection of flow equations

To simplify the problem, we start with incompressible flow, though our simulation is a low Mach number compressible flow. Thus, we have the equations

$$\begin{aligned} \frac{\partial u}{\partial x} + \frac{\partial v}{\partial y} &= 0 \\ \frac{\partial u}{\partial t} + u \frac{\partial u}{\partial x} + v \frac{\partial u}{\partial y} &= -\frac{\partial p}{\partial x} + \frac{1}{\text{Re}} \left(\frac{\partial^2 u}{\partial x^2} + \frac{\partial^2 u}{\partial y^2} \right) \\ \frac{\partial v}{\partial t} + u \frac{\partial v}{\partial x} + v \frac{\partial v}{\partial y} &= -\frac{\partial p}{\partial y} + \frac{1}{\text{Re}} \left(\frac{\partial^2 v}{\partial x^2} + \frac{\partial^2 v}{\partial y^2} \right). \end{aligned} \quad (9)$$

Denoting the velocity field by the vector $\mathbf{q} = (u \ v)^T$, the function $f(\mathbf{q})$ is therefore

$$f(\mathbf{q}) = C(\mathbf{q}, \mathbf{q}) + P + \frac{1}{\text{Re}} V(\mathbf{q}), \quad (10)$$

where

$$C(\mathbf{q}, \mathbf{q}) = \begin{pmatrix} -u \frac{\partial u}{\partial x} - v \frac{\partial u}{\partial y} \\ -u \frac{\partial v}{\partial x} - v \frac{\partial v}{\partial y} \end{pmatrix}, \quad P = \begin{pmatrix} -\frac{\partial p}{\partial x} \\ -\frac{\partial p}{\partial y} \end{pmatrix}, \quad V = \begin{pmatrix} \frac{\partial^2 u}{\partial x^2} + \frac{\partial^2 u}{\partial y^2} \\ \frac{\partial^2 v}{\partial x^2} + \frac{\partial^2 v}{\partial y^2} \end{pmatrix}. \quad (11)$$

Following the same definition, we will have $\mathbf{r} = (\tilde{u} \ \tilde{v})^T$, where

$$u(x, y, t) = \tilde{u}(x, g(t)y, t) \quad (12)$$

$$v(x, y, t) = \tilde{v}(x, g(t)y, t) \quad (13)$$

Then, it is straightforward to obtain $f_g(\mathbf{r})$ as

$$f_g(\mathbf{r}) = C_g(\mathbf{r}, \mathbf{r}) + P_g + \frac{1}{\text{Re}} V_g(\mathbf{r}), \quad (14)$$

where

$$C_g(\mathbf{r}, \mathbf{r}) = \begin{pmatrix} -\tilde{u} \frac{\partial \tilde{u}}{\partial x} - g \tilde{v} \frac{\partial \tilde{u}}{\partial y} \\ -\tilde{u} \frac{\partial \tilde{v}}{\partial x} - g \tilde{v} \frac{\partial \tilde{v}}{\partial y} \end{pmatrix}, \quad P_g = \begin{pmatrix} -\frac{\partial \tilde{p}}{\partial x} \\ -g \frac{\partial \tilde{p}}{\partial y} \end{pmatrix}, \quad V_g(\mathbf{r}) = \begin{pmatrix} \frac{\partial^2 \tilde{u}}{\partial x^2} + g^2 \frac{\partial^2 \tilde{u}}{\partial y^2} \\ \frac{\partial^2 \tilde{v}}{\partial x^2} + g^2 \frac{\partial^2 \tilde{v}}{\partial y^2} \end{pmatrix}. \quad (15)$$

We can write \mathbf{r} as an expansion in basis function as

$$\mathbf{r} = \phi_0(y) + \sum_{k=-\infty}^{+\infty} \sum_{n=-\infty}^{+\infty} a_{k,n}(t) \Phi_{k,n}(x, y). \quad (16)$$

where k is the wave number and n is the index for each POD mode, and $\phi_0(y)$ is the (scaled) mean flow

$$\phi_0(y) = U_\infty(1 + \tanh(2y))/2. \quad (17)$$

Typically, the basis functions $\Phi_{k,n}$ are chosen to be divergence-free, so that any linear combination of them is also divergence-free, and the continuity equation is automatically satisfied. One difficulty with the scaling procedure used here is that when the scaling is introduced, the resulting modes are not precisely divergence-free. To simplify the problem, this incompressibility constraint is removed in our modeling. Although there is no *a priori* justification for this, we will observe in section 2.4 that the errors introduced are small, since the velocity field computed by the model remains nearly divergence free. For more accurate models, one could imagine enforcing incompressibility by modeling the pressure term as in Noack et al.[26]

We proceed by considering only wave numbers $k = \pm 1$, and the first two POD modes $n = 1$ and $n = 2$ for each wave number:

$$\Phi_{k,n}(x, y) = e^{i(2\pi k/L)x} \phi_{k,n}(y), \quad k = \pm 1; \quad n = 1, 2, \quad (18)$$

where $\phi_{k,n}(y) = (\hat{u}_{k,n}(y) \ \hat{v}_{k,n}(y))^T$. The summation is then an approximation of the original \mathbf{r} , though the notation \mathbf{r} is still used for the summation in the rest of this paper without confusion. Moreover, the condition that \mathbf{r} be real gives

$$a_{1,1} \Phi_{1,1} + a_{1,2} \Phi_{1,2} = a_{-1,1}^* \Phi_{-1,1}^* + a_{-1,2}^* \Phi_{-1,2}^* \quad (19)$$

which permits further simplification.

To obtain equations for time coefficients $a_{1,1}(t)$ and $a_{1,2}(t)$, we need to project the equation

$$\frac{\partial \mathbf{r}}{\partial t} = f_g(\mathbf{r}) - \frac{\dot{g}}{g} y \frac{\partial \mathbf{r}}{\partial y} \quad (20)$$

onto modes $\Phi_{1,1}$ and $\Phi_{1,2}$. In this projection, we make another approximation that the contribution from the pressure terms is small due to our boundary conditions. As previously mentioned, improvements may be possible by modeling the pressure terms explicitly[26].

We also need the projection unto the “zero” mode $y\partial_y r_0$ to obtain the equation for the thickness change (see equation (8)).

Eventually, with only modes $(k, n) = (1, 1)$ and $(k, n) = (1, 2)$ retained, we have the equations for g , $a_{1,1}$, and $a_{1,2}$ as

$$\dot{g} = \frac{c_{01}}{n_0} a_{1,1} a_{1,1}^* g^2 + \frac{c_{02}}{n_0} a_{1,2} a_{1,2}^* g^2 + 2\text{Re}\left(\frac{c_{03}}{n_0} a_{1,1} a_{1,2}^*\right) g^2 + \frac{1}{\text{Re } n_0} \frac{d_0}{g^3}, \quad (21)$$

$$\dot{a}_{1,1} = \frac{c_{11} + g c_{12}}{n_1} a_{1,1} + \frac{c_{13} + g c_{14}}{n_1} a_{1,2} + \frac{1}{\text{Re}} \left[-\left(\frac{2\pi}{L}\right)^2 + \frac{d_1}{n_1} g^2 \right] a_{1,1} + \frac{e_1}{n_1} \frac{\dot{g}}{g} a_{1,1}, \quad (22)$$

$$\dot{a}_{1,2} = \frac{c_{21} + g c_{22}}{n_2} a_{1,1} + \frac{c_{23} + g c_{24}}{n_2} a_{1,2} + \frac{1}{\text{Re}} \left[-\left(\frac{2\pi}{L}\right)^2 + \frac{d_2}{n_2} g^2 \right] a_{1,2} + \frac{e_2}{n_2} \frac{\dot{g}}{g} a_{1,2}, \quad (23)$$

where all coefficients are constants (depending only on the modes), and are defined in appendix A.

If we choose two more modes $n = 1$ and 2 for wave number $k = 2$, the same derivation can give the equations of g , $a_{1,1}$, $a_{1,2}$, $a_{2,1}$, and $a_{2,2}$ to describe a more complex system discussed later. The resulting equations are lengthy, however, and are not shown here.

2.4 Results

As mentioned in section 2.2, the shear layer flow considered in this paper is started with a hyperbolic tangent velocity profile $u_0(x, y) = U_\infty(1 + \tanh(2y))/2$ with small perturbations, which are eigenfunctions of the most unstable modes calculated from the linear stability analysis. With different initial condition, the following two cases are studied. The first case has the most unstable $k = 1$ mode as the initial perturbation, and the flow is dominated by single $k = 1$ wave number as we expect. The second case has $k = 2$ mode as the initial perturbation, and is dominated by $k = 2$ mode at the beginning. However, the $k = 1$ mode grows naturally (initially excited by numerical noise) as it is more unstable than $k = 2$ mode when the shear layer spreads, so in this case both $k = 1$ and $k = 2$ modes are needed.

2.4.1 Flow with mode $k = 1$ only

Firstly, we consider the flow with an initial perturbation containing only the $k = 1$ wavenumber. The time evolution of the shear layer thickness is shown in figure 4. From this figure (with the help of flow visualization), we can easily identify three developing stages: (1) vortices with wave number $k = 1$ are rolling up and causing fast growth of the shear layer thickness; (2) the flow becomes stable as the shear layer thickens, vortices start to decrease in strength, and viscous dissipation starts to play the main role in the shear layer thickness spreading; (3) only the trivial solution (mean flow) remains, and the flow is simply spreading by viscous dissipation.

(k, n)	λ	energy (%)
(1, 1)	112.5	93.0
(2, 1)	3.6	3.0
(1, 2)	3.7	3.1
all $k = 0$		0.4

Table 1: Energy contained in different modes, for an initial condition with $k = 1$.

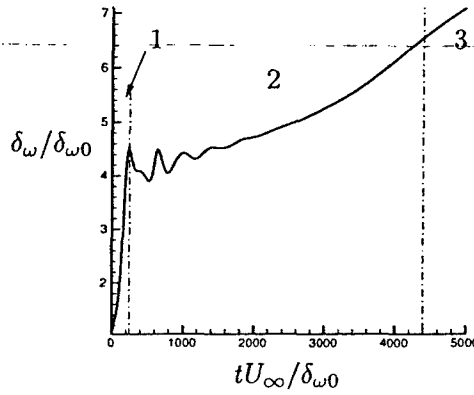


Figure 4: Vorticity thickness changes with time: three developing stages are marked.

To obtain a low-dimensional model, we must first choose appropriate basis functions. Because of the translation invariance in the x -direction, Fourier modes are an appropriate choice along the x -direction for our problem. Along the y -direction, we first scale all data snapshots to $\delta_g = a_g \delta_{\omega 0}$, where we choose $a_g = 4$ in our cases (this value is arbitrary, and chosen so that the scaled functions are well resolved on the computational grid). We then compute the POD modes of each wave number from the scaled data set. Table 1 shows that the first POD mode ($n = 1$) of $k = 1$ contains most of the energy (93.0%), the second POD mode ($n = 2$) of $k = 1$ and the first POD mode ($n = 1$) of $k = 2$ contain a small amount of energy, and the remaining modes contain very little energy. It is noticed that all $k = 0$ modes together take only 0.4% energy of the total, which indicates that the scaling has efficiently separated out the spreading of the mean flow.

Below, we will refer to the mode with, e.g., $k = 1$ and $n = 2$ as the (1, 2) mode. Notice from Table 1 that the (1, 2) and (2, 1) modes contain a small energy at about the same level. However, in forming reduced-order models, we notice that mode (1, 2) seems to be more dynamically important in the sense of catching the system evolution features with low-order models. Later, we will show that keeping only (1, 1) and (1, 2) can produce reasonably accurate models, while the same size model with (1, 1) and (2, 1) modes does not perform as well. These most dynamically important modes, (1, 1) and (1, 2) are shown in figures 5 and 6. It is noticed that

mode $n = 1$ and $n = 2$ have different symmetries.

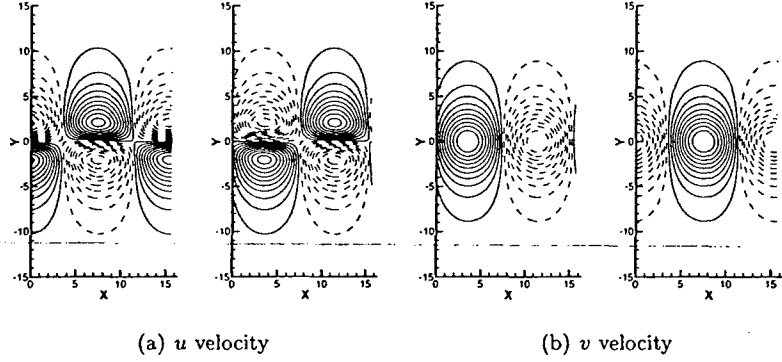


Figure 5: Two-dimensional picture of mode $(k,n) = (1,1)$ (—positive, ----negative): Real (left) and imaginary (right) parts of u and v velocity.

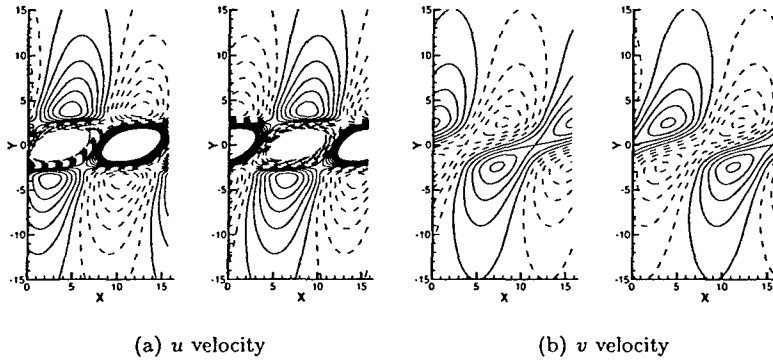


Figure 6: Two-dimensional picture of mode $(k,n) = (1,2)$ (—positive, ----negative): Real (left) and imaginary (right) parts of u and v velocity.

The time coefficients $a_{11}(t)$ and $a_{12}(t)$ of modes $(1,1)$ and $(1,2)$ respectively are shown in figure 7 (for all time coefficients a , only the real part is shown). Compared to the “ g ” thickness changing along time, we can clearly check the three developing stages defined before. Figure 7 also shows us an important relation between the phase difference between the two a coefficients and the thickness growth. Close inspection reveals that the thickness change (increase or decrease) is related to the phase difference of these two modes. Though the physical mechanism for this is not clear, observe from the figure that when the thickness is growing rapidly, the coefficients a_{11} and a_{12} are in phase, and the thickness is growing less rapidly or decreasing, these coefficients are out of phase.

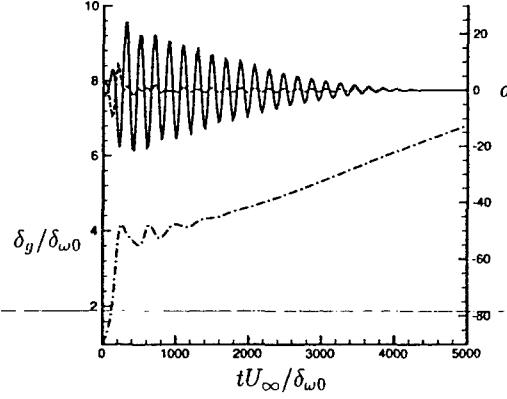


Figure 7: Projection of full simulation, for an initial perturbation with $k = 1$: time coefficients $a_{11}(t)$ and $a_{12}(t)$, and the shear layer thickness δ_g : — a_{11} ; --- a_{12} ; -.- δ_g .

Simulations of the 2-mode model, retaining only $(k, n) = (1, 1)$ and $(1, 2)$ modes, are shown in figure 8, for the same initial condition as in figure 7, and the qualitative features of these two figures are similar. However, the model result looks more “violent” than the simulation result, which, we believe, is damped by energy transfer to higher wave numbers.

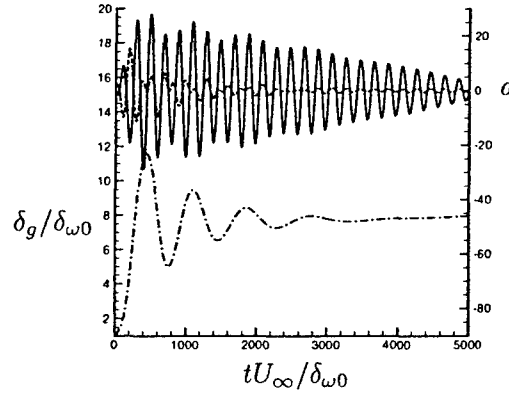


Figure 8: Simulation of 2-mode model, for an initial perturbation as in Fig. 7: time coefficients $a_{11}(t)$, $a_{12}(t)$, shear layer thickness δ_g : — a_{11} ; --- a_{12} ; -.- δ_g .

2.4.2 Flow with both modes $k = 1$ and $k = 2$

(k, n)	λ	energy (%)
(1, 1)	24.00	65.6
(2, 1)	10.75	29.4
(1, 2)	0.76	2.1
(2, 2)	0.61	1.7
all $k = 0$		1.8

Table 2: Energy contained in different modes, for an initial condition with $k = 2$.

The flow in the second case is dominated by structures with $k = 1$ and $k = 2$ at its different developing stages, and this case incorporates more interesting physical phenomena as well (e.g., vortex merging). The time evolution of the shear layer thickness for this flow is shown in figure 9, where we identify the whole history as five stages with comparison to the flow visualization from the DNS data: (1) $k = 2$ vortices roll up; (2) $k = 2$ modes become stable at this thickness; (3) $k = 1$ modes are introduced (primarily due to numerical noise), are more unstable, and cause vortex merging; (4) $k = 1$ modes become stable; (5) viscous dissipation dominates.

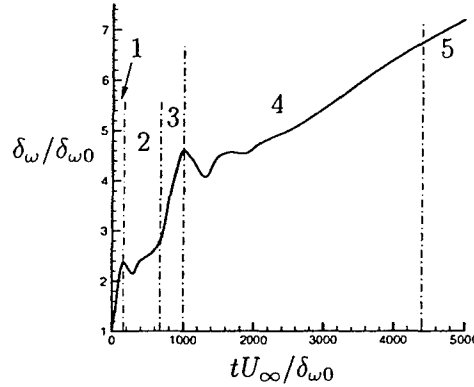


Figure 9: Vorticity thickness changes with time, for an initial perturbation with $k = 2$: five stages in the development are marked (see text for a description).

With the same rescaling and empirical mode decomposition, table 2 shows the energy budget of the modes from this more complex dataset. This time, the first POD modes of $k = 1$ and $k = 2$ share the most part of the energy, and the energy taken by all other modes is small. With the experience of $k = 1$ case, we can expect the importance of the second POD modes though the energy of them is small.

Figures 10–13 show the u and v components of the four most energetic modes, which together capture 98.8% of the total energy.

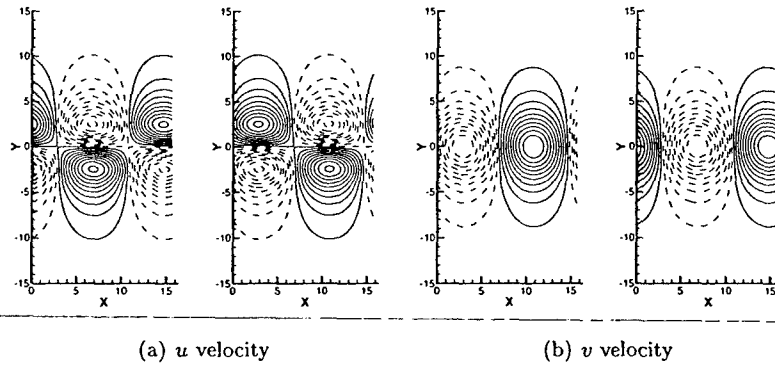


Figure 10: Two-dimensional picture of mode $(k,n) = (1,1)$ (—positive, ----negative): Real (left) and imaginary (right) parts of u and v velocity.

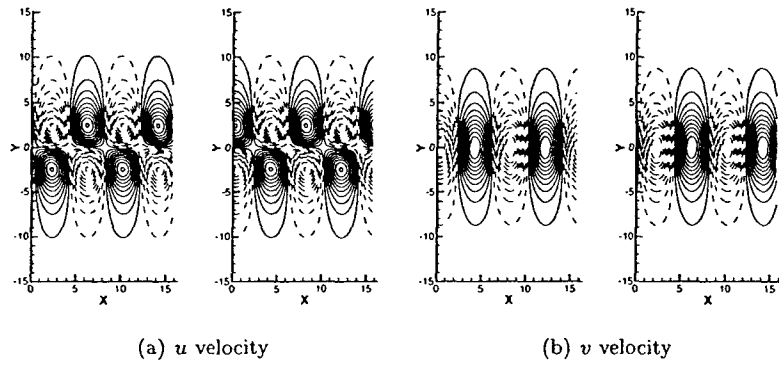


Figure 11: Two-dimensional picture of mode $(k,n) = (2,1)$ (—positive, ----negative): Real (left) and imaginary (right) parts of u and v velocity.

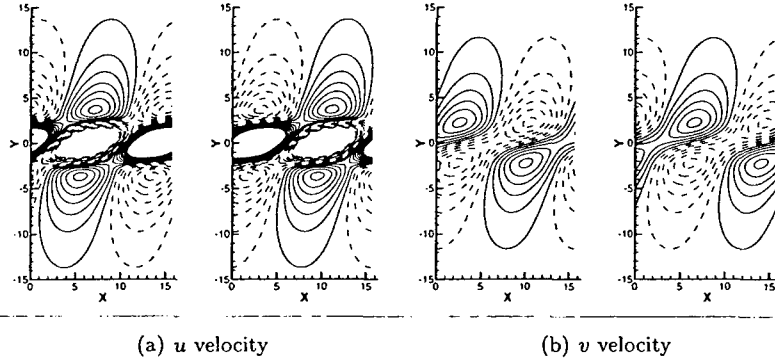


Figure 12: Two-dimensional picture of mode $(k, n) = (1, 2)$ (—positive, ----negative): Real (left) and imaginary (right) parts of u and v velocity.

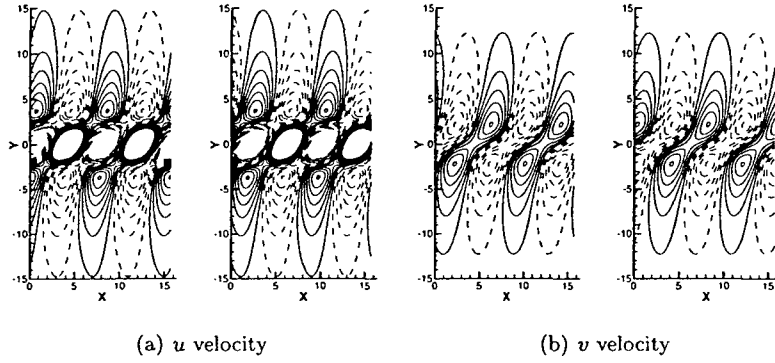


Figure 13: Two-dimensional picture of mode $(k, n) = (2, 2)$ (—positive, ----negative): Real (left) and imaginary (right) parts of u and v velocity.

Figure 14 shows the time coefficients of modes $(k, n) = (1, 1)$, $(1, 2)$, $(2, 1)$, and $(2, 2)$, computed by projecting the data from the full simulation. The figure clearly illustrates the five distinct stages of shear layer development described above: first the $k = 2$ vortices grow, then saturate and gradually damp; then the energy is transferred to the $k = 1$ mode (merging), until this too is damped and only viscous diffusion remains. As in the previous section, the phase difference between two POD modes at the same wave number can be observed as the corresponding shear layer thickness changes.

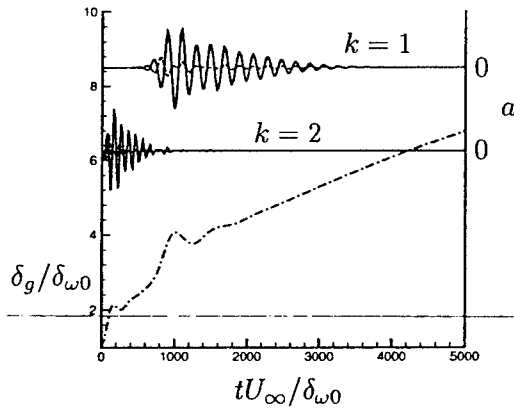


Figure 14: Projection of full simulation, initial perturbation with $k = 2$: time coefficients $a_{11}(t)$, $a_{12}(t)$, $a_{21}(t)$, and $a_{22}(t)$, and the shear layer thickness δ_g : — $n = 1$; ---- $n = 2$; $n = 3$; -.-.- $n = 4$.

Clearly, a 2-mode model will not be enough to describe this more complex system. We use the 4-mode model with $(k, n) = (1, 1)$, $(k, n) = (1, 2)$, $(k, n) = (2, 1)$ and $(k, n) = (2, 2)$ as shown in figure 15. This 4-mode model captures those dynamics already captured by 2-mode model, and in addition also describes the vortex merging process successfully.

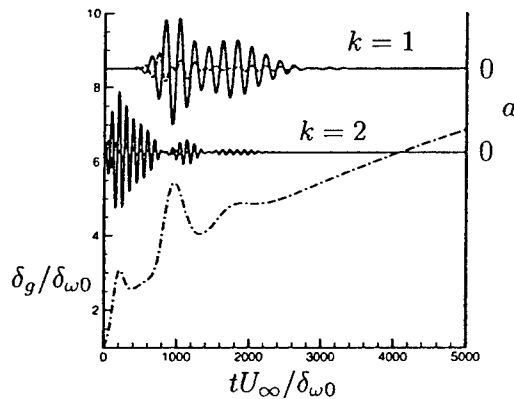


Figure 15: Simulation of 4-mode model, initial perturbation as in Fig. 14: time coefficients $a_{11}(t)$, $a_{12}(t)$, $a_{21}(t)$, and $a_{22}(t)$, and the shear layer thickness $\delta_g(t)$: — $n = 1$; ---- $n = 2$; $n = 3$; -.-.- $n = 4$.

Finally, because conservation of mass is not explicitly enforced with these scaled models, one should verify to what extent the models do preserve incompressibility.

Figure 16 shows the maximum divergence of the velocity field at each time, for the same initial conditions as the other figures in this section, and the variation from divergence-free is small but measurable. Although failure of a model to perfectly satisfy conservation of mass may seem disturbing, we are after only approximate models in the first place, so these small errors are acceptable. Note that in the scaled coordinates, the continuity equation becomes $\partial_x \tilde{u} + g \partial_y \tilde{v} = 0$. Also, recall that even the full simulation is not incompressible, but is a low-Mach-number compressible flow, so is not perfectly divergence free. It is possible that one could obtain improved models by scaling the amplitude of the v -component of velocity by g , so that in the scaled coordinates the continuity equation remains $\text{div } \mathbf{r} = 0$, but if this scaling is used, the pressure term does not drop out of the momentum equation, and would need to be modeled separately[26].

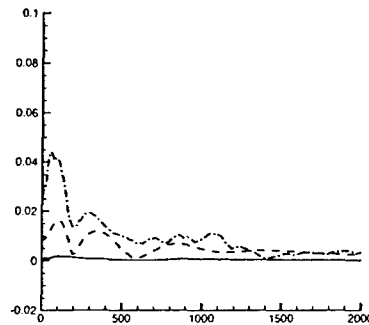


Figure 16: The incompressibility of the simulation data and model data: (—), DNS data $\partial u / \partial x + \partial v / \partial y$; (---), 2-mode model $\partial \tilde{u} / \partial x + g \partial \tilde{v} / \partial y$; (----); 4-mode model $\partial \tilde{u} / \partial x + g \partial \tilde{v} / \partial y$.

2.5 Summary and future work

The main goal of this section has been to obtain low-dimensional dynamical models that describe how a shear layer evolves in time: in particular, how unsteadiness in the shear layer (the growth of Kelvin-Helmholtz modes) affects the spreading rate of the shear layer, which in turn affects the growth or decay of the Kelvin-Helmholtz modes. A better understanding of these shear layer dynamics is essential for understanding effects of external forcing on free shear layers, and in turn cavity oscillations.

Using scaled POD and Galerkin projection, we can build a model based on a few basis functions to describe a temporally developing shear layer with its thickness growing in time. The basis functions are scaled (dynamically) in the y -direction so that in the scaled coordinates, the shear layer thickness remains constant in time. In our study, we noticed the dynamic importance of the second POD mode (for both wavenumbers $k = 1$ and 2), though it captures much less energy than the first POD

mode. We observe that the phase difference between the first and second POD mode plays a significant role in the shear layer spreading, and the growth in amplitude of the main energy-containing mode.

A 2-mode model is constructed by projection of incompressible Navier-Stokes equations onto the first and second POD modes with wavenumber $k = 1$. This model is simple and can describe the vortex roll-up, nonlinear saturation, and viscous damping when we applied it to a shear flow with a $k = 1$ mode as an initial perturbation. A more complex 4-mode model can also be obtained by projection onto the first and second POD modes of wavenumbers $k = 1$ and 2. Applying this model to a shear flow with a $k = 2$ mode as initial perturbation, we see a more accurate description than the 2-mode model, as we expect. More importantly, we see the 4-mode model successfully captures the vortex merging behavior, as eventually the $k = 1$ mode becomes more unstable. In the future, we hope to use models such as these to study the effects of external forcing (particularly high-frequency forcing), and ultimately to develop models suitable for feedback control, for instance to enhance or suppress spreading of the shear layer and growth of disturbances.

3 Subsonic cavity experiments

3.1 Experimental setup

A subsonic cavity model, wind tunnel nozzle and diffuser were constructed specifically for closed-loop control experiments at subsonic speeds. The test facility shown in Fig. 17 was installed at the Princeton University Gas Dynamics Lab in the November 2003. The test section is 6 inches long and 3 inches wide. The cavity floor is adjustable to allow $L/D = 2, 3, 4$ or 5. Benchmark experiments showed that subsonic Mach numbers up to $M = 0.76$ can be reached before the wind tunnel chokes. The upstream boundary layer thickness is approximately 0.3 inches thick at $M = 0.45$.

Acoustic tones measured in the cavity are compared with the predictions of Rossiter's formula in Fig. 18. Although there is some deviation between theory and experiment in the highest frequency resonant tone, the experimental results show good agreement up to $M = 0.55$. At higher Mach numbers a constant frequency "lock-on" type behavior is observed when the ceiling of the wind tunnel is acoustically reflective. After changing the sound absorption material on the top surface of the cavity from a closed-cell plastic to an open-celled acoustic foam, the "lock-on" behavior was suppressed. The data in Fig. 19 show very little evidence of lock-on, which indicates the transverse tunnel modes are weakened.

For closed-loop control experiments, the cavity floor and backwall are instrumented with Endevco pressure transducers to provide feedback signals. A Krohn-Hite bandpass filter, voicecoil actuator, and digital signal processor (dSPACE 1104) for the control algorithm complete the control system.

An accurate transfer function of the actuator is an essential component of any closed-loop control algorithm. A voicecoil type of actuator was chosen based on its high bandwidth and prior experience in [58]. The actuator consisted of a Selenium

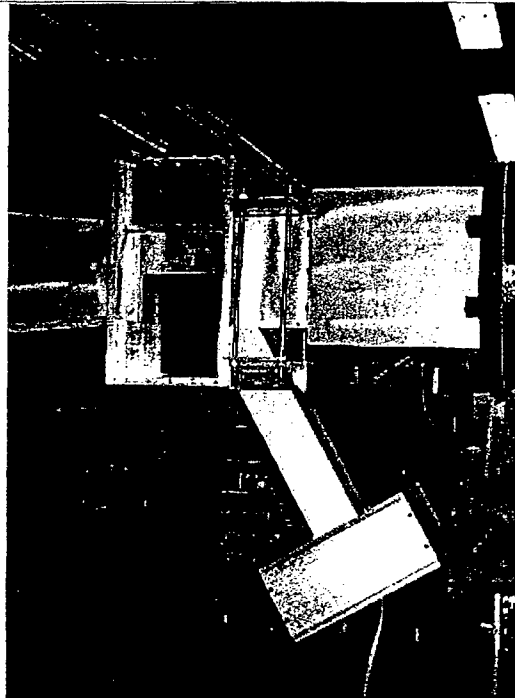


Figure 17: Photograph of cavity model and actuator installed at Gas Dynamics Lab.

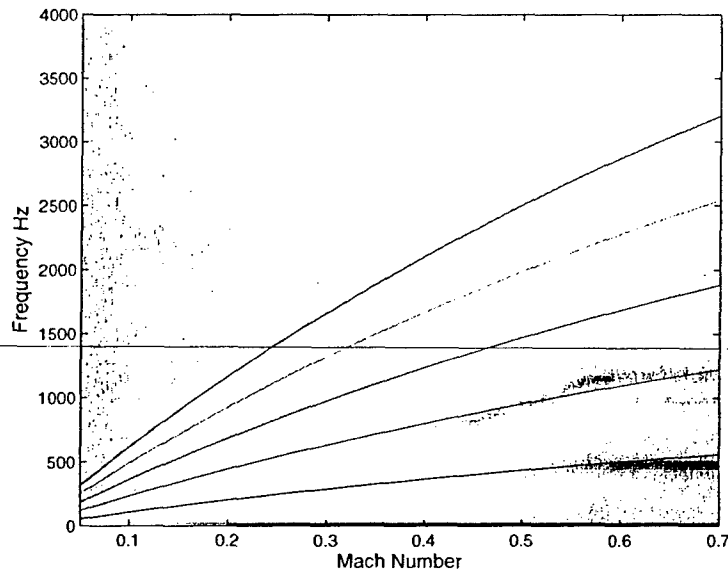


Figure 18: Acoustic tones measured in experiments and compared with Rossiter's equation with an acoustically "hard" ceiling in the tunnel. Note the "lock-on" of frequencies for $M > 0.55$.

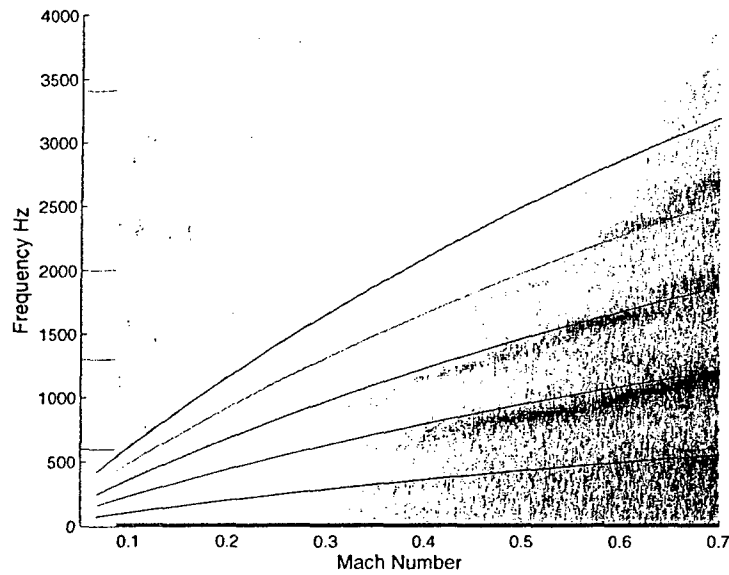


Figure 19: Acoustic tones measured in experiments and compared with Rossiter's equation with an acoustically "soft" ceiling using an open-celled acoustic foam. The lock-on seen in Fig. 18 is no longer present.

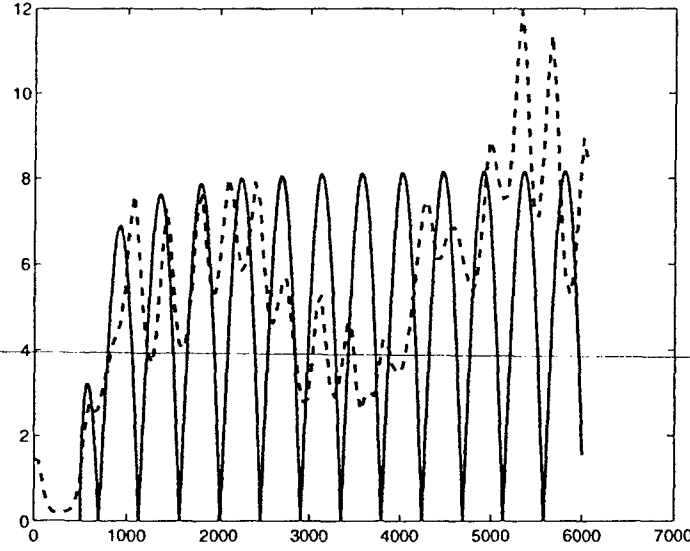


Figure 20: Comparison of actuator pressure/voltage transfer function (---) with pressure amplitude model based on an exponential Horn equation (—).

D405TI (200 W) compression driver connected to an inverted exponential horn. The exponential area variation of the horn was designed to provide a high cutoff frequency of 200 Hz, but experiments showed the actual cutoff frequency to be 500 Hz. A comparison of the experimentally measured pressure spectrum with a model of exponential horn transmitted pressure is shown in Fig. 20.

3.2 Results

3.2.1 Cavity response to open-loop and closed-loop forcing

Open-loop forcing experiments were done to determine the ability of the actuator to modify the flow. The actuator was set at a specific amplitude and frequency, while the freestream Mach number was varied from 0 to 0.67. The results in Fig. 21 when forcing at 1200 Hz show a detectable signal up to $M = 0.55$. One can clearly see the suppression of surrounding modes when the cavity is forced to oscillate at the 1200 Hz forcing frequency.

Although it had been generally accepted that the cavity resonant tones are self-excited, [36] provided strong evidence that many of the Rossiter modes are actually weakly damped oscillators. Weakly damped modes are driven by external disturbances, and are thus fundamentally different from self-excited modes. On the other hand, single-mode resonances that have been observed in a number of cavity experiments appear to be self-excited. The single mode resonance occurred when the Rossiter modes coincided with the longitudinal modes in the cavity. However, by extending the analysis of a recent theoretical model for acoustic resonances, [2]

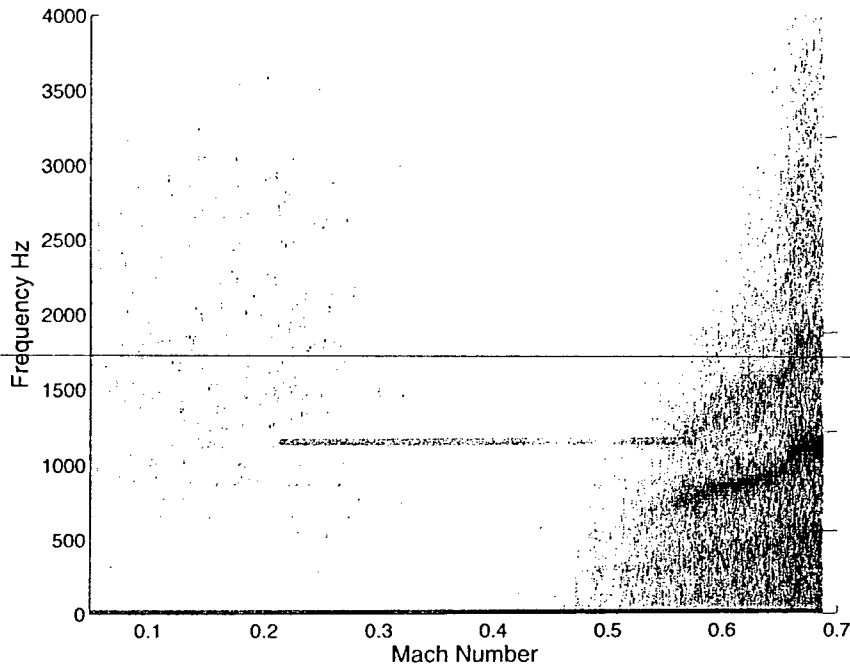


Figure 21: Spectrogram of open loop forcing at 1200 Hz shows good actuator authority up to $M = 0.55$.

determined that single mode behavior cannot come from longitudinal mode coupling. Instead, they suggest Rossiter mode coupling with transverse acoustic modes between the wind tunnel ceiling and cavity floor.

Closed-loop forcing experiments were done to provide data for controller and model development. A wide range of flow and controller conditions were explored. A sample of the closed loop control results is shown in Fig.22 where a baseline spectrum at $M = 0.45$ freestream condition is compared with a case of closed loop control. A digital controller was used with a time delay of 0.00021 sec. The passband on the filter settings was 660 Hz to 1.3 kHz.

Approximately 12 dB of suppression occurred in the principal Rossiter mode. Some reduction of the broadband occurred, suggesting the mean flow was modified by the forcing.

In order to determine whether the oscillations observed are self-sustained or lightly-damped resonances, sustained by external disturbances, the probability density function (PDF) of the pressure signal was examined, as done in our previous work [37]. Specifically, the pressure data were narrowband filtered about the resonant peak, using a 4th-order discrete-time Butterworth filter with a passband of 820–840 Hz (filtered both forward and backward in time to remove phase errors), and then a histogram of the filtered signal was calculated. The resulting probability density is shown in Fig. 23, along with a normal distribution with the same variance.

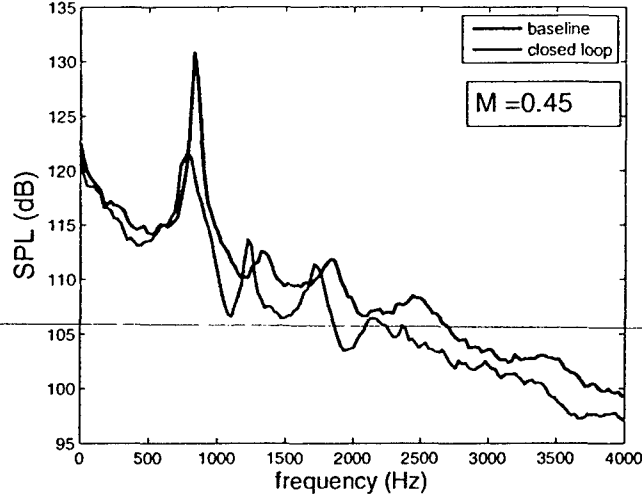


Figure 22: Comparison of closed loop control (red) with the unforced cavity spectrum at $M = 0.45$ (blue).

The approximately normal distribution shows that the oscillations in this case result from amplification of disturbances by a lightly-damped resonance, rather than a self-sustained oscillation, for which the distribution would have two peaks (see [37] for more information about this method of determining the oscillation regime).

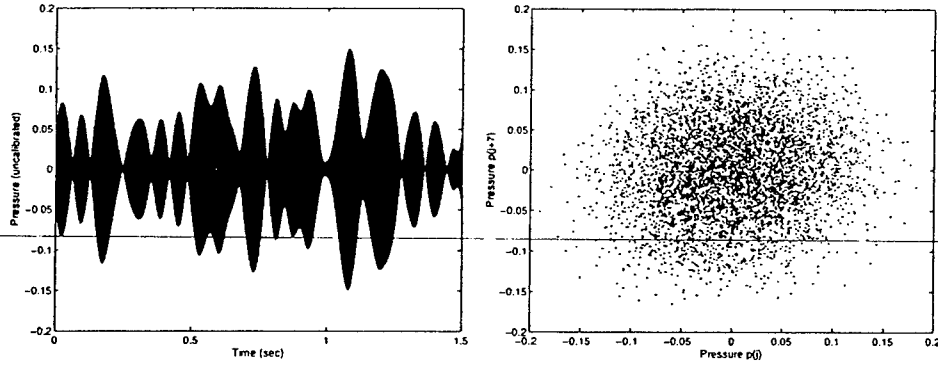
3.2.2 System identification and linear models

Because the oscillations in the present experiment appear to result from amplification of disturbances, rather than a self-sustaining limit cycle, it is likely one can model the cavity as a linear system. The transfer function from the actuator to the measured pressure signal was identified by forcing the actuator with sinusoids with frequency sweeping from 100 Hz to 4 kHz, and measuring the resulting response at $M = 0.45$. The resulting transfer function, and its coherence, is shown in Fig. 24. The coherence is small at frequencies at which the actuator authority is low relative to the magnitude of external disturbances (which are amplified by the resonant cavity flow), and at these frequencies the transfer function estimate is less reliable.

One can use the estimated transfer function to predict the response of the cavity experiment to closed-loop control. If the transfer function from the (unknown) disturbance signal $d(s)$ to the pressure transducer is denoted $P_d(s)$, and the transfer function from the (known) actuator input $u(s)$ to the same pressure transducer is $P_u(s)$, then the overall pressure signal $y(s)$ is

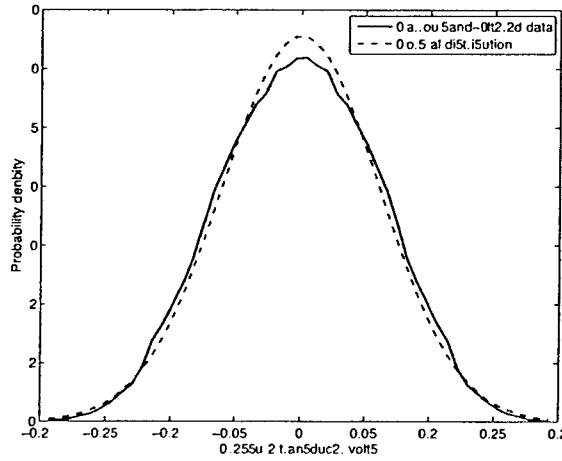
$$y = P_d(s)d + P_u(s)u. \quad (24)$$

Without feedback ($u = 0$), the pressure signal is just $y = P_d(s)d$. With a feedback



(a) Filtered signal

(b) Phase portrait



(c) Probability density

Figure 23: (a) Pressure signal from the unforced cavity experiment at $M = 0.45$, narrowband filtered about the resonant frequency of 830 Hz, showing the random envelope of the amplitude of the 830 Hz oscillations. If oscillations were self-sustained, the envelope would be more constant in amplitude. (b) and (c) make these observations more quantitative, showing the phase portrait and probability density function of the filtered pressure signal (—), compared with a normal distribution (----). The phase portrait concentrated in the center (as opposed to a ring) with approximately normal distribution indicates that oscillations result from amplified disturbances, rather than self-sustained oscillations.

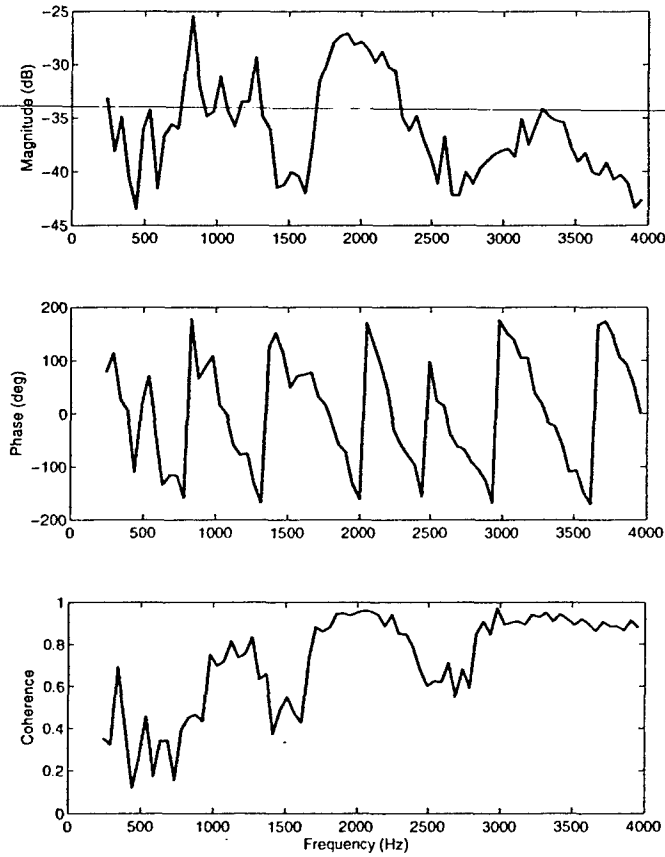


Figure 24: Transfer function from actuator (volts) to center floor pressure transducer (volts) for cavity experiment at $M = 0.45$, measured from experiments with sinusoidal forcing, and corresponding coherence.

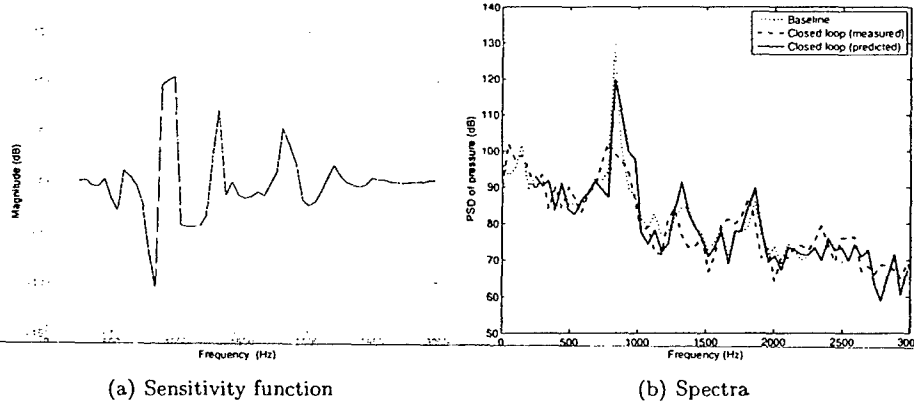


Figure 25: (a) Sensitivity function S , computed from measured cavity transfer function at $M = 0.45$ and controller with passband of 660–1300 Hz, and delay of 0.00021 sec. (b) Comparison of predicted and measured closed-loop spectra, and baseline (no forcing).

$u(s) = C(s)y(s)$, where $C(s)$ is a known controller, (24) becomes

$$y = \frac{P_d(s)}{1 - P_u(s)C(s)}d,$$

so the resulting y is changed, relative to the open-loop system, by the factor

$$S(s) = \frac{1}{1 - P_u(s)C(s)},$$

called the *sensitivity function*. We have determined $P_u(s)$ from the system identification experiment described above (Fig. 24), and $C(s)$ is known (it is our choice), so we can predict $S(s)$, and therefore predict the closed-loop response to disturbances.

Fig. 25 shows the sensitivity function, for the controller used in Fig. 22, with a gain of 5 (in the experiment, the gain is set by the position of a knob on an analog amplifier, so this value is not precisely known). The corresponding prediction of the closed-loop response is shown along with the measured closed-loop response in Fig. 25. While the quantitative agreement is not perfect, presumably due to inaccuracies in identifying the transfer function $P_u(s)$, the qualitative agreement is good.

3.3 Summary

This section summarized the results of subsonic experiments conducted at the Gas Dynamics Laboratory at Princeton, in the Mach number range 0–0.67. Spurious tunnel modes present in the initial experiments were suppressed using an open-celled ceiling foam, and after this modification, the measured frequencies of oscillation

matched the expected Rossiter modes. The response of the actuator, a zero-net-mass device, agreed with predicted response using an exponential horn equation, and maintained authority up to $M = 0.55$. Closed-loop experiments were able to suppress the oscillations by approximately 12 dB, using a bandpass filter and time delay as a controller. The oscillations for these flow conditions were shown to result from amplification of disturbances, rather than self-sustained oscillations, and linear models based on this mechanism produced a good qualitative agreement with the experimental results.

4 Supersonic cavity experiments

Many active flow control techniques have demonstrated the ability to suppress tones, particularly at subsonic speeds. The key strategy in all cases is to disrupt the Rossiter feedback mechanism. Passive, active open-loop, and closed-loop control approaches have shown varying degrees of success. Cattafesta, et al.[4] and Colonius[8] provide extensive reviews of active flow control techniques used, and discussions of the physical mechanisms involved in controlling cavity tones.

Active control with open-loop forcing of the shear layer attempts to suppress tones by forcing at a non-resonant frequency. Sarno and Franke[40], Shaw[43, 44], Samimy, et al.[39], and Cattafesta, et al.[5] have shown the ability to suppress cavity tones with the open loop approach. Cattafesta, et al.[5] compared suppression by closed-loop flow control to the open-loop case, and demonstrated that the closed-loop approach used an order of magnitude less power.

The mechanism by which open-loop forcing of the shear layer suppresses the resonant tones is not understood. Why, for example, when the shear layer is excited by a non-resonant frequency, would not the forcing frequency simply superpose on the baseline spectrum? Apparently some type of nonlinear interaction occurs between the base flow state and the forcing field, which interferes with the resonance mechanism. At least five different arguments for the open-loop suppression mechanism can be found in the literature, and have been itemized below. The sixth mechanism in the list refers to linear wave cancelation that can only occur with a closed-loop control system.

1. Lifting the shear layer which changes the downstream reattachment point[52, 3] - modification of mean shear profile combined with lifting[54]
2. Change of shear layer stability characteristics by thickening the shear layer [8, 53]
3. Low-frequency excitation of the shear layer at off-resonance condition [40, 3, 5, 11, 27, 42]
4. High-frequency (hifex) excitation[53, 42]- accelerated energy cascade in inertial range "starves" lower frequency modes[45] - mean flow alteration, which changes stability characteristics [47]
5. Oblique shock flow deflection and reduction of longitudinal flow speed [38]

6. Cancellation of feedback acoustic wave [5, 6]

The suppression mechanisms listed above are primarily intuitive, and do not offer much predictive capability. Progress toward developing a predictive model of the effect of shear layer thickening and the change in stability characteristics is discussed in detail by Colonius[8]. Sahoo, et al.[38] developed a physics based model to explain the mechanism by which micro-jets suppress cavity resonance in a supersonic flow. By considering the effect of an oblique shock formed at the leading edge of the cavity by the micro-jets, they were able to estimate the flow deflection angle and speed reduction effects. Their model correlated very well with the experimental data.

The objective of this supersonic flow experiment was to get a better understanding of the cavity response to open-loop forcing by systematically varying the forcing frequencies and amplitudes. The effect of dynamic pressure could be studied by changing the wind tunnel stagnation pressure. Our initial expectations were to find nonlinear interactions between the forcing field and the base state resonant modes, similar to the subsonic case, but this did not happen. The following sections describe the calibration of the pulsed-blowing actuator used for the forcing, and the pressure measurements of the cavity response when the forcing amplitude and frequency and dynamic pressure were varied.

4.1 Experimental setup

The supersonic cavity experiments were conducted in the supersonic wind tunnel at the Illinois Institute of Technology Fluid Dynamics Research Center. The facility is a blow-down wind tunnel with a variable throat area. The test section is 102 mm wide and 114 mm high. The Mach number was fixed at $M=1.86$ for this study and $U_\infty=629 \pm 19$ m/s. Wind tunnel stagnation pressures (absolute) ranged from 0.31 MPa to 0.72 MPa. Operating the wind tunnel at different stagnation pressures made it possible to change the static and dynamic pressure in the test section, while keeping the Mach number fixed. The stagnation temperature in the wind tunnel was 290 K. The unit Reynolds number at $M=1.86$ was 49×10^6 per meter.

The cavity model was machined into the floor of the test section as shown in Fig.26. The sidewall of the wind tunnel was removed for this photograph to expose the details of the cavity and actuator nozzle block. The pulsed-blowing air from the siren valve enters through the side of the wind tunnel and enters the plenum of the nozzle block seen on the left side of the cavity.

The cavity is 152 mm long, 102 mm wide and 30.5 mm deep, giving it $L/D = 5$ and $L/W = 1.5$. Pressure fluctuations inside the cavity were recorded with two Kulite XCS-093 transducers located in the center span of the cavity floor at 8.25 mm and 144 mm from the upstream cavity wall. The boundary layer thickness approaching the leading edge of the cavity was estimated from schlieren images and a boundary layer rake of total pressure probes to be $\delta = 8$ mm.

The pulsed-blowing actuator consisted of a compressed air supply, siren valve and nozzle block. The siren valve manufactured by Honeywell was connected to the side of the nozzle plenum with a 75 mm long tube, giving a bandwidth of approximately 1.5 kHz. Two interchangeable nozzle blocks were constructed with different exit

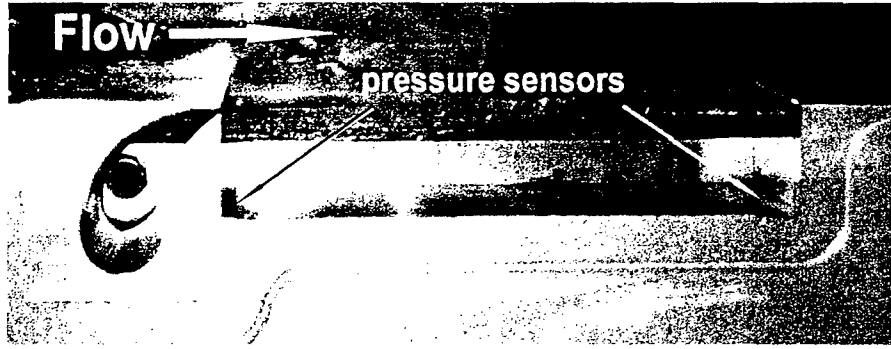


Figure 26: Photograph of cavity model in supersonic wind tunnel. The nozzle block is visible on the left (upstream) side of the cavity.

angles, one exiting parallel to the flow direction and the other at 45° relative to the downstream direction. For both nozzles the exit spanned the width of the cavity and had a height of 3.2 mm.

Pulsed-blowing actuators require some flow through the system in order to produce oscillations, but with careful tuning of the plumbing system it is possible to generate oscillation amplitudes larger than the mean flow speed, producing instantaneously reversed flow. The actuator performance was documented using both a hot-wire anemometer to measure velocity at the slot exit, and a Kulite pressure transducer to measure the instantaneous pressure in the slot exit of the actuator nozzle. The face of the Kulite pressure sensor was oriented directly at the exit of the actuator to record the instantaneous total pressure. Time series traces of the velocity and pressure at 750 Hz forcing frequency with an actuator supply pressure of 124 kPa (absolute) are shown in Fig. 27.

Velocity measurements of the mean velocity and root mean square (r.m.s.) velocity at the exit of the actuator are shown in Fig. 28a. The forcing frequency was set at 750 Hz, while the supply pressure was varied from 101 kPa to 240 kPa. The velocity oscillation amplitude saturates as the supply pressure to the actuator is increased, while the mean velocity increases monotonically. This type of behavior is common for pulsed-blowing actuators. Attempts to increase oscillation amplitude by increasing the supply pressure often do more to increase the mean flow than the oscillatory component of velocity.

The corresponding mean and r.m.s. pressure values at the actuator exit are shown in Fig. 28b. The mean pressure steadily increases with supply pressure, while the r.m.s. pressure grows at a much slower rate. The mean flow through the actuator is expressed as a blowing coefficient, B_c as defined in the following equation. Following Zhuang, et al. [60] the reference area is defined as the cavity length times cavity width.

$$B_c = \frac{\rho_{jet} A_{jet} U_{jet}}{\rho_\infty A_{ref} U_\infty} \quad (25)$$

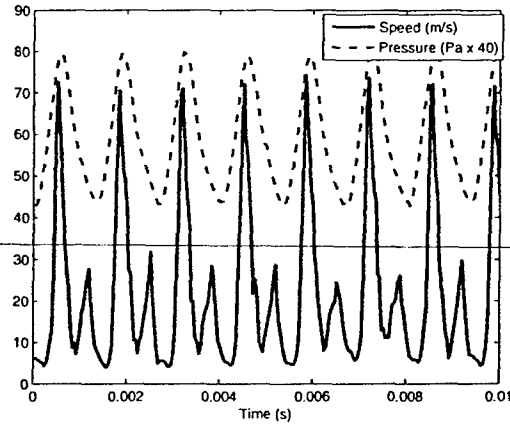


Figure 27: Velocity (solid line) and pressure (dashed line) time series at actuator exit plane. Actuator supply pressure = 124 kPa, frequency = 750 Hz

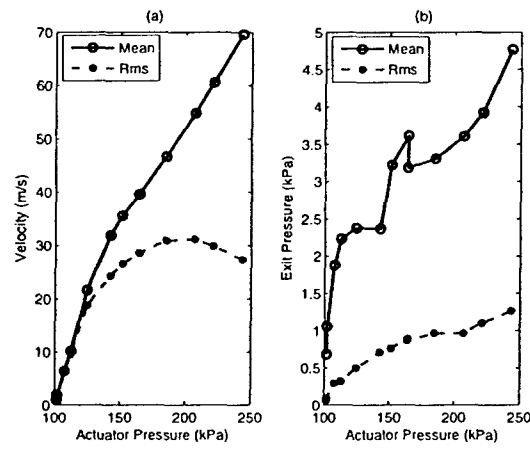


Figure 28: Supply pressure dependence of the mean and r.m.s. pressures measured at the actuator exit plane with 750 Hz forcing frequency.

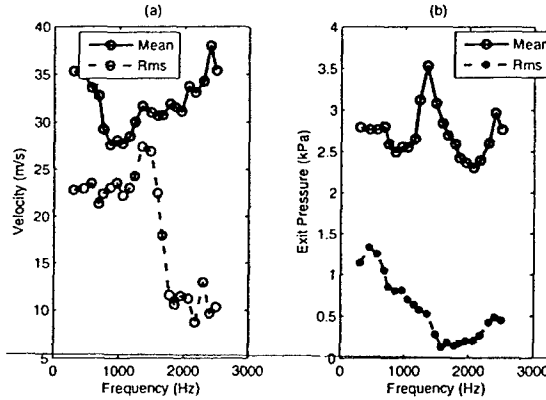


Figure 29: Frequency dependence of the mean and r.m.s. velocities measured at the actuator exit plane with a 138 kPa input pressure ($B_c = .0010$).

The output from the pulsed-blowing actuator was strongly dependent of the forcing frequency. To document the frequency response of the actuator, the siren valve frequency was varied from 400 Hz to 2500 Hz, while maintaining a nominally constant input pressure of 138 kPa. Figure 29a shows a sharp cutoff in the r.m.s. velocity fluctuation amplitude near 1500 Hz. The r.m.s. pressure shown in Fig. 29b has a more gradual decay in amplitude with frequency.

4.2 Results

The fluctuating pressure was recorded with transducers in the floor of the cavity. The baseline response without forcing is presented in Sect.3.1. The response of the cavity to the open-loop forcing at different frequencies and amplitudes is described in Sect.3.2.

4.2.1 Baseline cavity behavior - no forcing

The supersonic cavity control experiments by Zhuang, et al.[60] measured a linear dependence of the overall sound pressure level with wind tunnel stagnation pressure. A similar linear dependence was found in this experiment as shown in Fig.30 for supersonic flow. At stagnation pressures below 300 kPa the flow was subsonic in the wind tunnel.

Pressure spectra measured by the upstream pressure sensor are shown in Fig.31 for different wind tunnel stagnation pressures. Without forcing six identifiable Rossiter modes can be found in the spectra. The best fit of the Rossiter equation (1) to the data was obtained using $\alpha=0.2$ and $\kappa=0.4$. The predicted mode frequencies are indicated by the vertical lines in Fig.31. A close look at the figures shows that increasing the wind tunnel stagnation pressure does not affect the resonant frequencies, but does increase the amplitude of the spectral peaks.

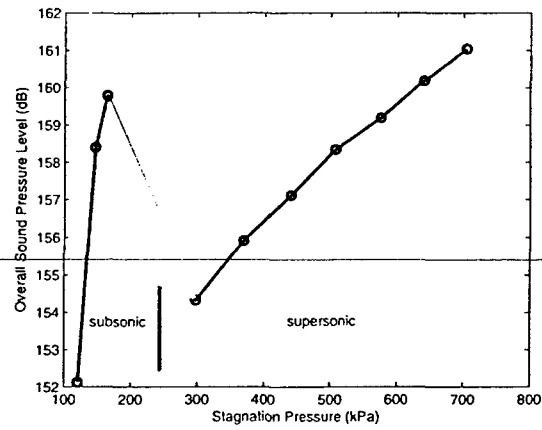


Figure 30: Overall sound pressure level increases linearly with stagnation pressure in the supersonic flow regime.

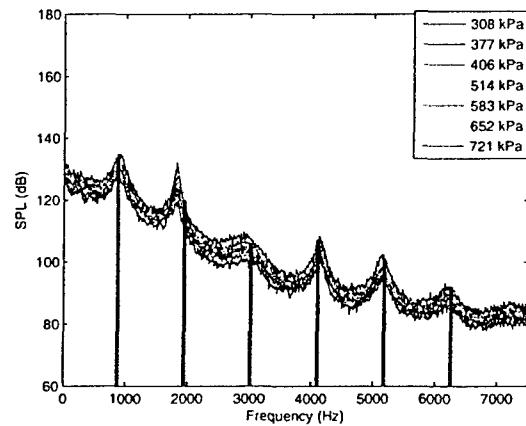


Figure 31: Pressure spectra with no forcing are superposed. Each spectrum increases in amplitude as the wind tunnel stagnation pressure (values shown in the legend) is increased.

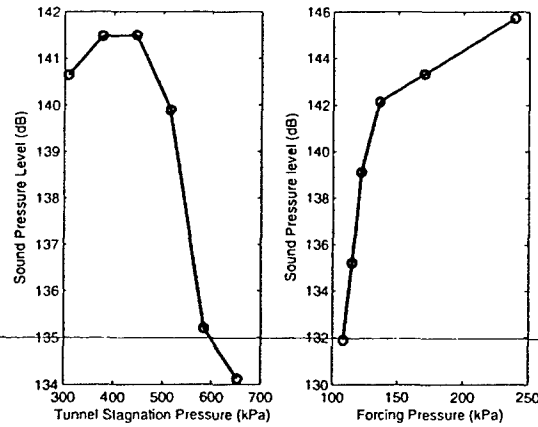


Figure 32: Decay and growth of the 800 Hz spectral peak amplitude with: a) changing wind tunnel stagnation pressure (actuator supply pressure = 101.6 kPa); b) changing actuator supply pressure (wind tunnel stagnation pressure = 584 kPa). Actuator frequency = 800 Hz

4.2.2 Cavity response to periodic forcing

The performance of pulsed-blowing actuators is dependent on the pressure difference between the supply pressure and the pressure at the actuator nozzle exit. Increasing the wind tunnel stagnation pressure increases the static pressure in the test section, which may reduce the effectiveness of the pulsed-blowing actuator. A plot of 800 Hz peak amplitude against the wind tunnel stagnation pressure at fixed forcing amplitude is shown in Fig.32a. Above a stagnation pressure of 450 kPa the cavity response decreases with the dynamic pressure. Similarly, the dependence of the 800 Hz peak amplitude on the actuator supply pressure is shown in Fig.32b. Initially the peak growth is proportional to actuator supply pressure, then the cavity response begins to saturate at actuator pressures above 140 kPa. This behavior is consistent with the saturation of the fluctuating velocity levels seen in Fig.28. It can be shown that the actuator response scales with the pressure difference across the actuator.

The pulsed-blowing actuator was set to a frequency of 1000Hz and a supply pressure of 170kPa. The wind tunnel stagnation pressure was fixed at 584 kPa, giving a static pressure in the test section close to the calibration conditions. The pressure spectrum measured before the wind tunnel was started is shown in Fig.33 as the dashed line. The spectrum obtained with the wind tunnel running at $M=1.86$ is superposed in the figure as a solid line. The input from the actuator was amplified 25 dB above the no-flow condition by the cavity.

There was some concern that the sharp peak in the spectrum at the forcing frequency was not a fluid dynamic response of the cavity, but possibly an acoustic signature of the actuator, such as, a simple superposition of the forcing field. To check this, the forcing frequency and amplitude were varied, and the response of the

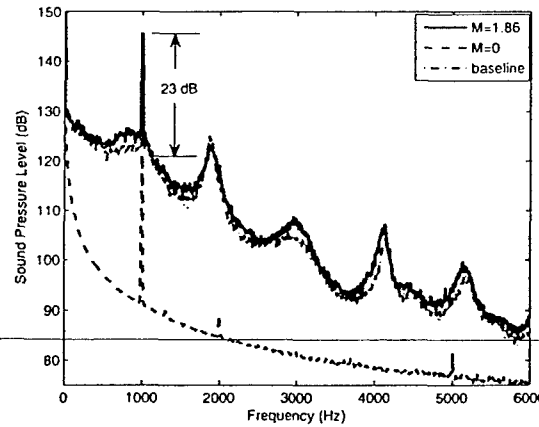


Figure 33: Comparison of pressure spectra at 1000 Hz forcing frequency (dashed line is for no flow in wind tunnel and solid line is for supersonic flow) shows amplification by the flow. Wind tunnel stagnation pressure = 584 kPa and actuator supply pressure = 170 kPa ($B_c = .0013$).

cavity measured to get a better understanding of the nature of the forcing peak.

The actuator frequency was changed to 800 Hz, slightly below the first Rossiter mode at 880 Hz. The amplitude of the pulsed-blowing actuator was changed by adjusting the supply pressure. The pressure spectra are superposed in Fig.34a along with the baseline (no-forcing) case. Each spectrum corresponds to a different supply pressure to the actuator. The growth of the unsteady forcing peak with increasing supply pressure can be seen. We also found that nonlinear mode interactions (combination modes) do not appear, which is significantly different behavior than the subsonic flow case.

The 800 Hz peak amplitude with supersonic flow is plotted against the forcing amplitude in the quiescent wind tunnel in Fig.34b. The dashed line has a slope of 1.0, which implies a linear relationship between the forcing and response amplitudes. The data appear to be close to displaying a linear relationship.

Next the forcing frequency was changed to 1300 Hz, which was between the first and second Rossiter mode. Figure35 compares the baseline spectrum (quiescent wind tunnel) with the forced case. At this frequency the cavity response is lower than the acoustic forcing level without flow in the tunnel, indicating that the cavity system is attenuating the disturbance.

The forcing frequency was varied from 500 Hz to 2400 Hz in 100 Hz increments, while maintaining a constant input pressure to the actuator of 170 kPa. The measured spectra are superposed in Fig.36a. The response contains both the frequency response of the actuator and that of the cavity system. At the lower forcing frequencies near the first Rossiter mode, the actuator frequency response is reasonably constant (see Fig.29), and the response of the cavity follows the peak seen in the unforced spectrum. As the frequency is increased toward the second Rossiter mode,

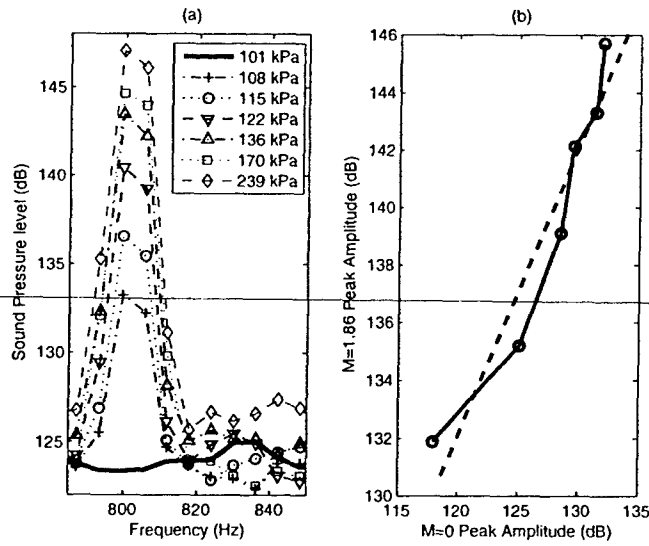


Figure 34: Growth of the 800 Hz peak with increasing forcing amplitude- a) spectral peak increases with changing actuator supply pressure; b) peak response amplitude plotted against the pressure measured in the quiescent cavity.

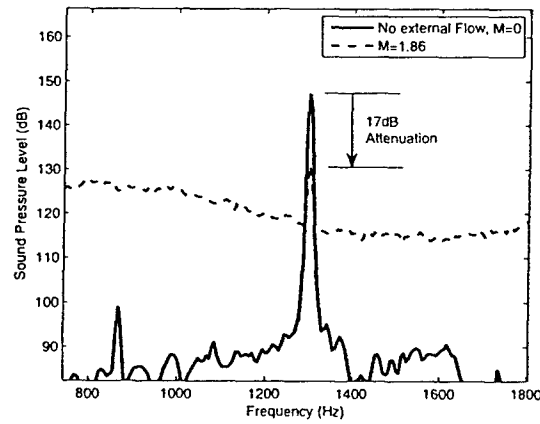


Figure 35: 1300 Hz forcing amplitude shows attenuation between Rossiter modes. Actuator supply pressure = 170 kPa ($B_c = .0013$).

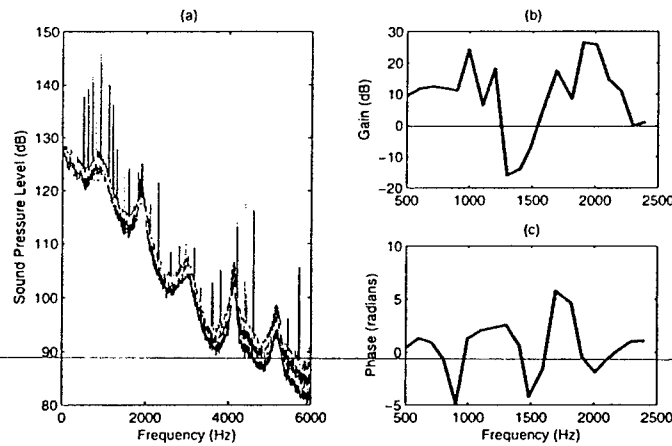


Figure 36: Effect of different forcing frequencies on spectrum with constant actuator supply pressure - a) spectrum; b) gain; c) phase

the amplitudes of the cavity response decrease for two reasons. First the actuator frequency response decreases (Fig.29), and second, as shown in the previous figure, the cavity system is attenuating disturbances between the Rossiter modes relative to the input disturbance amplitude.

To isolate the cavity system dynamics from these measurements it is necessary to account for the actuator frequency response. To do this, we measured the peak amplitude at each forcing frequency in the quiescent wind tunnel, $M=0$. The "gain" was defined as the difference between the dB level of the peak amplitude with the tunnel running and the quiescent tunnel measurement. The gain is shown in Fig.36b. Positive gain is seen around the first two Rossiter mode frequencies, and negative values corresponding to attenuation are located between the Rossiter modes. The corresponding phase between the actuator oscillations and the oscillating pressure field is plotted in Fig.36c.

4.2.3 Closed-loop cavity response

Closed-loop control of the supersonic cavity tones was done using an analog gain and phase control system. The feedback signal was provided by a Kulite pressure sensor in the upstream cavity wall. The control system gain was set by the power amplifier. The controller phase was adjusted with an analog phase-shift circuit and was set near 180° . The a small reduction in the peak of the second Rossiter mode can be seen along with an extraneous peak introduced by the analog controller, Fig. ?? . The level of suppression is increased as the gain to the amplifier increases, but the controller introduces additional modes into the system. To our knowledge this is the first demonstration of closed loop control of Rossiter tones in a supersonic cavity flow.

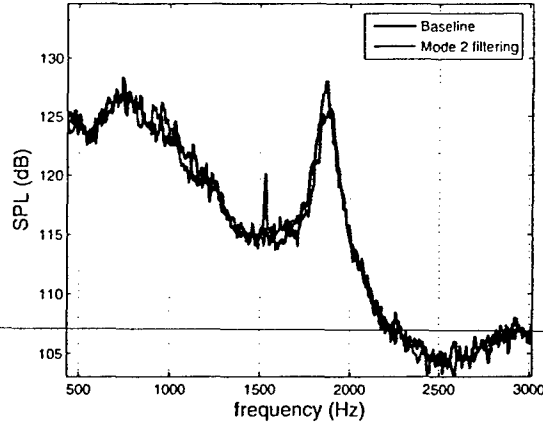


Figure 37: Closed-loop control of the 2nd Rossiter mode. The baseline and feedback with two gain settings are shown.

5 Subsonic numerical simulations

In this section, we present techniques for developing low-order models, and corresponding strategies for feedback control, using high-fidelity numerical simulations. Low-order models are obtained using two methods (empirical Galerkin models, and a simple nonlinear oscillator model), and validated against 2D direct numerical simulations of the flow, which is actuated by a body force at the leading edge of the cavity. This body force actuation is representative of the zero-net-mass actuation used in the subsonic experiments, as the actuator can impart a net momentum to the flow, with no net mass addition. The models are used to construct dynamic observers, which reconstruct the flow state from a single pressure sensor, and perform much better than static estimators (e.g., Linear Stochastic Estimation) commonly used for flow estimation. Several control approaches are compared, including simple proportional control with a phase lag, LQG control using Galerkin models, and a dynamic phasor approach based on the work of Noack et al [24]. All three controllers are implemented in the full simulation, and are able to reduce the amplitude of oscillations. The LQG regulator requires careful tuning, and the closed-loop behavior often does not match that predicted by the model, but the dynamic phasor approach eliminates the oscillations completely in the full simulation, with a transient response that matches that predicted by the low-order model.

The focus of this section is on developing low-order models useful for control design. Since the equations governing the general, arbitrary motion of a fluid are nonlinear and high-dimensional (turbulent solutions exist), low-order models are necessarily valid only over a limited dynamic envelope, typically for a small region of phase space, and for a narrow range of frequencies. In this paper, we explore two different types of models, and control design techniques: empirical Galerkin models, with controllers designed using linear techniques such as LQR/LQG; and dynamic

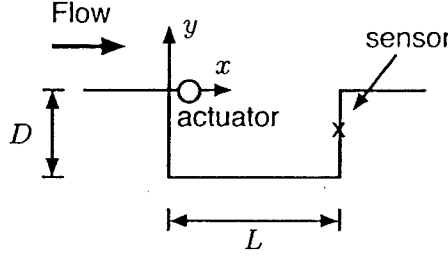


Figure 38: Cavity flow geometry, showing location of sensor and actuator.

phasor models, after [24, 48], which are simple enough that custom-tailored control laws may be constructed that respect the range of validity of the models.

The models and feedback laws we obtain are tested on a Direct Numerical Simulation (DNS) of the two-dimensional flow geometry shown in Fig. 38. The flow conditions used here are for a Mach number of 0.6, $L/D = 2$, $Re_\theta = 56.8$ based on momentum thickness θ at the cavity leading edge, and $L/\theta = 52.8$. This simulation has been carefully validated using grid resolution and boundary placement studies, and comparison with experimental data [30]. The grid used 1008×384 gridpoints above the cavity and 240×96 gridpoints inside the cavity, which is sufficient to resolve all of the scales at this Reynolds number.

The organization of the section is as follows: in §5.1 we describe the empirical Galerkin model, and the dynamic observer and Linear Quadratic Regulator we obtain from it, and compare this controller to a simple proportional feedback, with a phase shift. In §5.2, we describe a model based on dynamic phasors, based on the approach in [24, 48], and the controller and observer based on this model.

5.1 Empirical Galerkin models

Galerkin models are obtained by projecting known dynamics (e.g., the Navier-Stokes equations) onto a smaller-dimensional subspace. Here, we start with the *isentropic* Navier-Stokes equations [31], written in two spatial dimensions as

$$\begin{aligned}\frac{\partial a}{\partial t} &= -v \cdot \nabla a - \frac{\gamma - 1}{2} a \nabla \cdot v \\ \frac{\partial v}{\partial t} &= -v \cdot \nabla v - \frac{2}{\gamma - 1} a \nabla a + \nu \nabla^2 v,\end{aligned}\tag{26}$$

where $v = (v_1, v_2)$ is the velocity, a is the local sound speed (which may be related to other flow variables, such as pressure, via isentropic relations), γ is the ratio of specific heats (1.4 for air), and ν is the kinematic viscosity, assumed constant (small density variations). These equations are quadratic in the flow variables, of the form

$$\dot{q} = L(q) + Q(q, q),\tag{27}$$

where $q = (v_1, v_2, a)$, L is a linear operator, and Q is bilinear (linear in each argument).

In order to include actuation in the model, we represent the actuator as a body force in the momentum equation. With actuation included, then, the model has the form

$$\dot{q} = L(q) + Q(q, q) + \sum_{j=1}^p B_j u_j \quad (28)$$

where L and Q are the same as in (27), and where $B_j(x, y)$ denotes the (spatially-dependent) body force introduced by the j -th actuator $u_j(t)$. Here, we will use a single actuator, with B_1 oriented vertically (i.e., a body force in the y -direction), nonzero in a localized region in the shear layer (see Fig. 38), and zero elsewhere.

We expand the flow variables $q(x, y, t)$ in terms of basis functions $\varphi_j(x, y)$, as

$$q(x, y, t) = \bar{q}(x, y) + \sum_{j=1}^n z_j(t) \varphi_j(x, y), \quad (29)$$

where $\bar{q}(x)$ is some constant flow (typically a steady solution of Navier-Stokes, if known, or in our case a mean flow), and the z_j are time-varying coefficients. Thus, the *state* is the vector of coefficients $z = (z_1, \dots, z_n)$, and determining the state vector $z \in \mathbb{R}^n$ specifies the entire flow field q , according to (29). A *model* is then an evolution equation for $z(t)$.

Using the expansion (29), the model (28) has the form

$$\dot{z}_i(t) = c_i + A_{ij} z_j(t) + Q_{ijk} z_j(t) z_k(t) + B_{ij} u_j(t) \quad (30)$$

(summation implied), where

$$\begin{aligned} c_i &= \langle L(\bar{q}) + Q(\bar{q}, \bar{q}), \varphi_i \rangle \\ A_{ij} &= \langle L(\varphi_j) + Q(\bar{q}, \varphi_j) + Q(\varphi_j, \bar{q}), \varphi_i \rangle \\ Q_{ijk} &= \langle Q(\varphi_j, \varphi_k), \varphi_i \rangle \\ B_{ij} &= \langle B_j, \varphi_i \rangle, \end{aligned}$$

where we have assumed the basis functions φ_j are orthonormal.

Generically, (30) may have many equilibrium points (e.g., even in one dimension, it may have zero, one, or two equilibria, or a continuum in degenerate cases), but for the cases we investigate, \bar{q} in (29) will already be “close” to an equilibrium point (albeit an unstable one), which will imply that c_i is small, and there is a unique equilibrium point z^* close to the origin. In developing controllers, we will want to linearize about this equilibrium point, so writing $z(t) = z^* + \tilde{z}(t)$, one obtains

$$\dot{\tilde{z}}_i = \tilde{A}_{ij} \tilde{z}_j + Q_{ijk} \tilde{z}_j \tilde{z}_k + B_{ij} u_j, \quad (31)$$

where $\tilde{A}_{ij} = A_{ij} + (Q_{ijk} + Q_{ikj}) z_k^*$, so the linearized system is simply

$$\dot{\tilde{z}}_i = \tilde{A}_{ij} \tilde{z}_j + B_{ij} u_j. \quad (32)$$

5.1.1 Dynamic observers

For implementation, it is not feasible to measure the state vector z_j directly, so one must reconstruct the state from available sensor measurements, such as wall pressure. The sensor used in the observer is a pressure sensor in the downstream wall of the cavity, at $y = -0.5D$ (see Fig. 38). This sensor location was not optimized in any way, although one could consider optimal sensor placements by choosing sensor locations where the magnitudes of POD modes are large [7]. Each POD mode φ_j has a corresponding pressure p_j at this sensor location, and we represent the sensor signal $\eta(t)$ as

$$\eta(t) = \sum_{j=1}^n \tilde{z}_j(t) p_j = C \tilde{z}(t) \quad (33)$$

where C is the row vector $[p_1 \cdots p_n]$.

For the model given by (31), one needs to specify basis functions φ_j , $j = 1, \dots, n$. For the observer design, we take $n = 4$ and determine the basis functions by Proper Orthogonal Decomposition (POD) of a dataset of snapshots from the natural (unforced) flow, and these four modes were sufficient to capture over 95% of the energy in the fluctuations [31].

We then design a Kalman filter [59] for the linearized system $\dot{z} = \tilde{A}z$, where \tilde{A} is the matrix from (31). Letting \hat{z} denote the estimate of the actual state \tilde{z} , the observer has the form

$$\dot{\hat{z}} = \tilde{A}\hat{z} + L(\eta - C\hat{z}) \quad (34)$$

where L is a matrix with n rows and one column (in general, if m sensors are available, L has m columns). For the Kalman filter design, the process noise variance is estimated from the size of the nonlinear terms in (31). There is very little noise in the pressure measurements in the simulation, but we expect much greater noise in experiments, so we artificially add random noise to the sensor signal, and use this noise variance for designing the Kalman filter gains. Once the observer weights are designed, we consider both the linear observer (34) and the nonlinear observer obtained by adding the correction $L(\eta - C\hat{z})$ to the nonlinear system (31).

5.1.2 Model-based control design

Control design from Galerkin models is more challenging than observer design, because once actuation is introduced, typically the relevant flow structures change, so the basis functions φ_j need to include greater variety of spatial structures. To determine a model for control design, new POD modes were obtained from a richer variety of snapshots, taken from simulations incorporating actuation using a heuristic, proportional feedback from the pressure sensor in the downstream wall at $y = -0.5D$ (this heuristic feedback law is described below). The first 10 POD modes were used, which together capture over 99.99% of the energy in the controlled flow.

The equations were then linearized about an equilibrium point of the model (30), and a state feedback $u = Kz$ was found using LQR. Several different weights in the LQR cost function were tried and implemented in the full DNS simulation, and most stabilized the model quite rapidly, but were less effective on the full simulation:

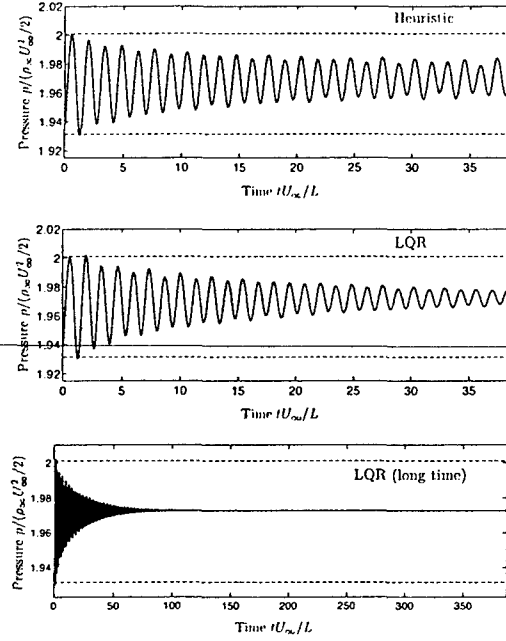


Figure 39: Time traces from full DNS simulation: heuristic, proportional control (top), LQR (middle), and LQR for longer time scale (bottom). Red dashed lines indicate the extent of oscillations in the unforced flow.

usually the controller reduced the oscillation amplitude for a few cycles, but then the amplitude would grow larger than without forcing. Careful tuning could yield controllers which performed well on the full simulation, and the results of one of these are shown in Fig. 39, along with a heuristic, proportional controller, for comparison.

The heuristic control law was obtained by prescribing the body force to oppose the local velocity of the shear layer: if the shear layer has a positive vertical velocity, the body force is downward. The local velocity of the shear layer at the actuation point was correlated with the wall-pressure measurement, which was used as the sensor for the controller, and the corresponding phase delay was included in the feedback law.

As shown in Fig. 39, the LQR controller performs slightly better than the proportional controller. However, the results of the full simulation do not match those predicted by the model (not shown), in which the feedback brings the amplitude close to zero with a settling time of about 2 cycles. The disagreement between model and full simulation is not surprising, however, because of the limited range of validity of the Galerkin models. Less aggressive LQR designs have little effect on the simulation, and more aggressive designs drive the system out of this range of validity. It is significant, however, that the feedback law shown in Fig. 39 stabilizes the full simulation for long time: these results indicate that stabilization is indeed possible for this flow, which is not necessarily the case for other flows, such

as cylinder wakes [24].

5.2 Dynamic phasor models

An alternative approach to modeling, inspired by the work of Tadmor, Noack, and others [24, 48, 25, 49], is to ignore the Navier-Stokes equations altogether, and postulate a low-order model that captures the relevant dynamical features of the flow. For instance, a simple dynamical system that describes oscillations at a frequency $\omega > 0$, is given by

$$\begin{aligned}\dot{r} &= \sigma r - \alpha r^3 \\ \dot{\theta} &= \omega\end{aligned}$$

where $\alpha > 0$ and σ are constants. In Cartesian coordinates, with $(a_1, a_2) = (r \cos \theta, r \sin \theta)$, and introducing a forcing term $u(t)$, the model takes the form

$$\dot{a} = A(r)a + Bu, \quad (35)$$

where $a = (a_1, a_2)$, $r = |a|$, and

$$A(r) = \begin{pmatrix} \sigma - \alpha r^2 & -\omega \\ \omega & \sigma - \alpha r^2 \end{pmatrix} \quad B = \begin{pmatrix} b_1 \\ b_2 \end{pmatrix}.$$

A model similar to this has been used for controlling cylinder wakes in [24, 48, 25, 49]. With no forcing ($u = 0$), with $\sigma \leq 0$, the origin is globally asymptotically stable, and with $\sigma > 0$, the origin is unstable, and there is a stable periodic orbit given by $r = \sqrt{\sigma/\alpha}$. This model is, of course, crude, and misses many of the details of the dynamics of cavity oscillations, but the goal is to obtain a model which is sufficient for control design, not to describe the cavity dynamics in a detailed way.

The parameters σ, α, ω are tuned to match simulations with no forcing, by observing the transient growth of oscillations from an initial condition near the unstable equilibrium point (of Navier-Stokes). The forcing parameters b_1, b_2 are then tuned to match simulations with small-amplitude sinusoidal forcing at a frequency close to the natural frequency ω .

5.2.1 Controller design

We wish to design a controller that stays within the range of validity of our model. Here, after [49], we consider a control input that is a sinusoid at the same frequency as the natural flow, with suitably chosen phase, and slowly-varying amplitude. In polar coordinates, (35) becomes

$$\begin{aligned}\dot{r} &= (\sigma - \alpha r^2)r + (b_1 \cos \theta + b_2 \sin \theta)u \\ \dot{\theta} &= \omega + \frac{1}{r}(b_2 \cos \theta - b_1 \sin \theta)u\end{aligned} \quad (36)$$

Now, let

$$u = r_c \cos(\theta - \theta_c),$$

where θ_c and r_c are controller parameters to be chosen. Assuming r is slowly varying, and inputs u are small, one may average over $\theta \in [0, 2\pi]$ (see [14]), and obtain the averaged equations

$$\begin{aligned}\dot{r} &= (\sigma - \alpha r^2)r + g_r \\ \dot{\theta} &= \omega + \frac{g_\theta}{r},\end{aligned}\tag{37}$$

where

$$\begin{aligned}g_r &= \frac{r_c}{2}(b_1 \cos \theta_c + b_2 \sin \theta_c) \\ g_\theta &= \frac{r_c}{2}(b_2 \cos \theta_c - b_1 \sin \theta_c).\end{aligned}$$

If \dot{r} and $\dot{\theta} = \omega$ in (36) are $O(\epsilon)$, then the averaging theorem states that solutions of (37) are ϵ -close to solutions of (36) for times $t \in [0, 1/\epsilon]$. Choosing θ_c so that

$$\cos \theta_c = \frac{b_1}{|b|}, \quad \sin \theta_c = \frac{b_2}{|b|},$$

one obtains

$$g_r = r_c \frac{|b|}{2}, \quad g_\theta = 0.$$

One possible choice for r_c is then $r_c = -2\kappa r/|b|$, under which the closed-loop averaged equations (37) become

$$\begin{aligned}\dot{r} &= (\sigma - \kappa - \alpha r^2)r \\ \dot{\theta} &= \omega.\end{aligned}\tag{38}$$

By choosing $0 < \kappa < \sigma$, the amplitude of the periodic orbit decreases to $\sqrt{(\sigma - \kappa)/\alpha}$, and if $\kappa > \sigma$, then the origin becomes globally attracting, at least for the model. In the control design, however, we must not be too aggressive with the choice of κ , or we may leave the range of validity of the model.

5.2.2 Observer design

In order to implement the controller above, one needs estimates of r and θ . We use a very simple linear estimator, assuming $\dot{r} = 0$ in (37), to obtain an observer of the form

$$\begin{pmatrix} \dot{\hat{a}}_1 \\ \dot{\hat{a}}_2 \end{pmatrix} = \begin{pmatrix} 0 & -\omega \\ \omega & 0 \end{pmatrix} \begin{pmatrix} \hat{a}_1 \\ \hat{a}_2 \end{pmatrix} + \begin{pmatrix} b_1 \\ b_2 \end{pmatrix} u + \begin{pmatrix} L_1 \\ L_2 \end{pmatrix} (\eta - \hat{a}_1),\tag{39}$$

where η is the sensor measurement, which we have assumed measures a_1 directly (we may always change coordinates so that this is the case). Without inputs or sensor corrections, the model (39) has a one-parameter family of periodic orbits, all with period $2\pi/\omega$, so with sensor corrections, this model should track oscillations of any amplitude and phase, as long as the frequency is close to ω . For stability, we choose $L_1 > 0$, and choosing $L_2 = \omega - L_1^2/2\omega$ gives good transient behavior (critically damped poles of the error dynamics).

Full simulations reveal that, when control is introduced, the mean value of the sensed pressure drifts slowly, so a high-pass filter was used to remove this nonzero mean component.

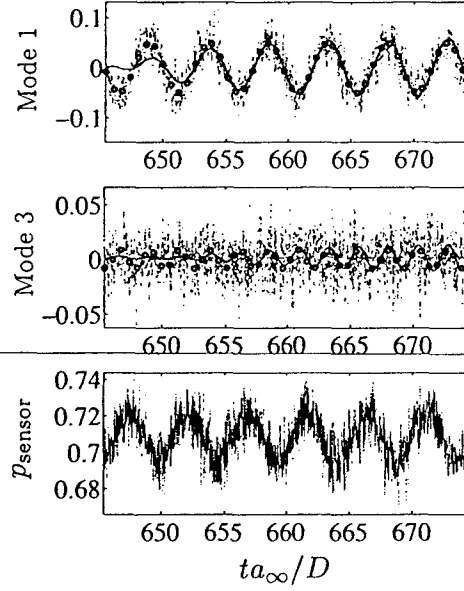


Figure 40: Time traces of pressure sensor and POD modes 1 and 3, for exact projection of DNS (black \circ), linear observer using 1 sensor (red dashed); nonlinear observer using 1 sensor (blue solid); and LSE using three sensors (green dashed).

5.3 Results

5.3.1 Comparison of dynamic and static observers

In Fig. 40, we compare the performance of the Kalman filter with a commonly used method for state estimation in fluids, known as Linear Stochastic Estimation (LSE) [1, 15], which has recently been applied to cavity flows [22, 23], as well as cylinder wakes [7] and other flows [13]. In this method, one correlates sensor signals with full flow field information from a known database, and then uses the correlation to predict flow field information from the sensor information, when the flow field is not directly available. Higher-order correlations are also possible, and Ukeiley has shown that quadratic stochastic estimation (QSE) outperforms LSE in predicting cavity flow fields [23].

The time traces shown in Fig. 40 show that both linear and nonlinear observers perform well, and accurately reconstruct the state from a single noisy pressure sensor. The nonlinear observer estimates the coefficients of mode 3 better, indicating that nonlinear coupling between modes 1–2 and modes 3–4 may be significant.

Figure 41 shows reconstructions of the full flow state at a particular time instant, comparing the full DNS solution with the estimate from the Kalman filter using a single (noisy) sensor, and LSE using three (noisy) sensors. The observer closely reproduces the flow structures in the full simulations. If clean sensors are used, the estimate from LSE is very close as well, but as seen in Fig. 41, when sensor noise is

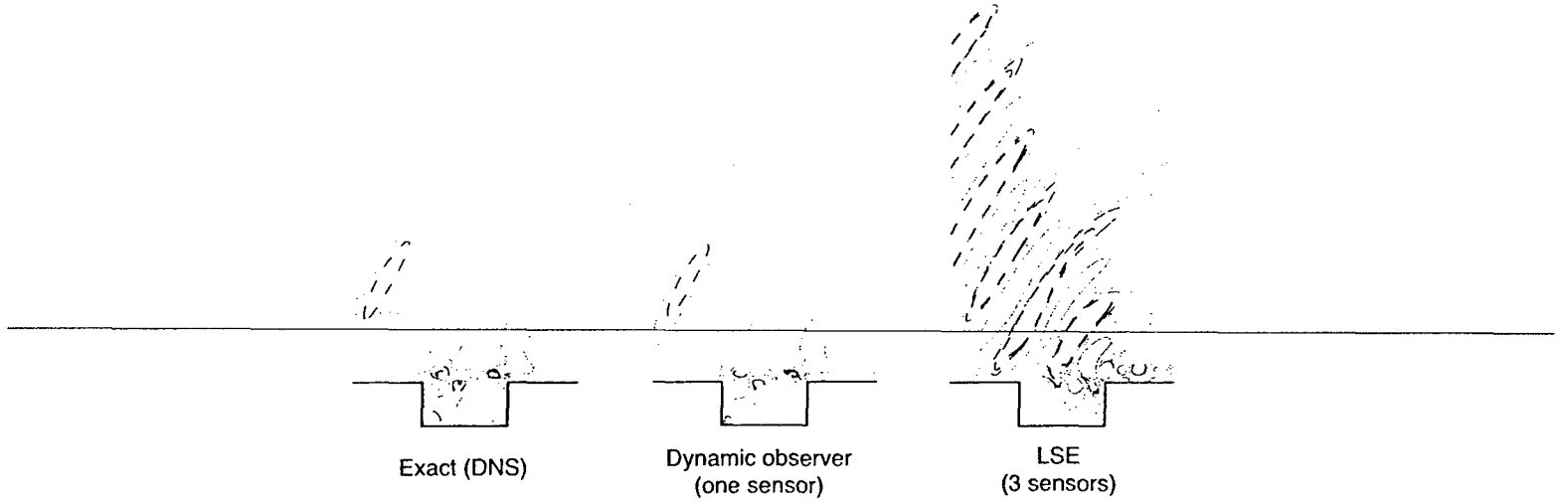


Figure 41: Instantaneous contours of dilatation, from exact simulation (left), and estimates from dynamic observer (center) and Linear Stochastic Estimation (right), using noisy pressure signals.

introduced, LSE can deviate substantially.

5.3.2 Closed-loop control in full simulations

Figure 42 shows the results of a controller and observer with $\kappa = 2\sigma$, and $L_1 = 1$. The behavior predicted by the model (38) is shown, and compared to the results of the full DNS simulation. The full simulation matches the model well, and remarkably, the amplitude of oscillations continues to decrease until a steady state is reached. The full simulations have been run until time $t = 120$, in the units in Fig. 42, and oscillations are virtually eliminated by time $t = 60$. The steady state reached is shown in Fig. 43, and looks similar to the time average of the uncontrolled flow. Different gains were also tried in the full simulation. For $\kappa/\sigma = 0.5$, the amplitude of oscillations was reduced, but not eliminated, while for $\kappa/\sigma \in [1, 3]$ the oscillations were eliminated completely. For $\kappa = 5\sigma$ the controller was too aggressive, and increased the amplitude of oscillations, deviating from the behavior predicted by the model.

As the Mach number varies, the frequency of oscillation changes, so one would not expect this controller to be very robust to changes in Mach number. Figure 44 shows the behavior of the controller designed for $M = 0.6$, when used at off-design flow conditions. As shown, for $M = 0.55$, the controller increases the amplitude of oscillations, while for $M = 0.65$ and 0.70 , the controller reduces the amplitude slightly, but does not stabilize.

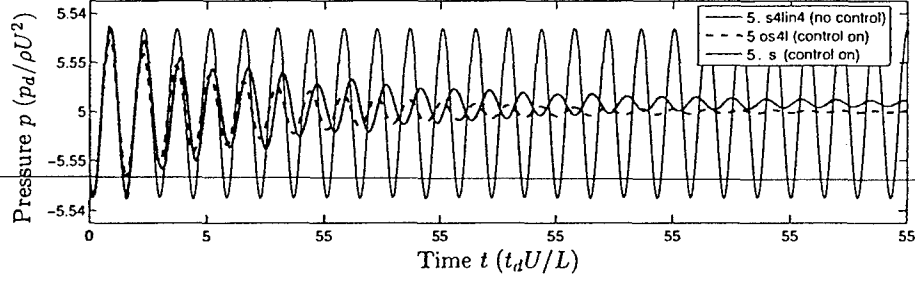


Figure 42: Dynamic phasor controller: No forcing (black solid), model (blue dashed), and full DNS (red solid), with $\kappa = 2\sigma$.

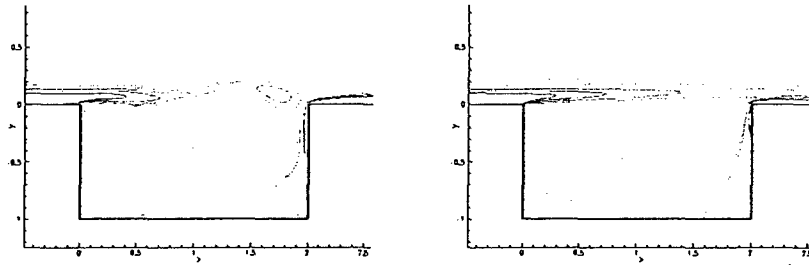


Figure 43: Instantaneous vorticity contours before controller is turned on (left), and with phasor-based controller (right). The flow at right is steady, indicating that this is an equilibrium of Navier-Stokes, stabilized by the controller.

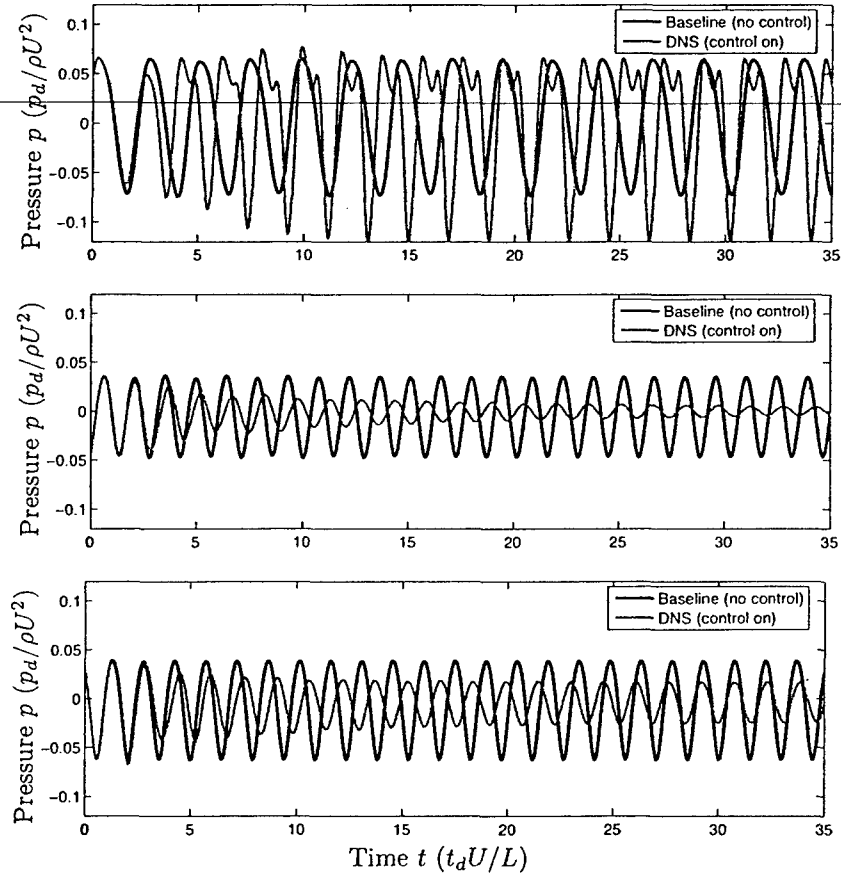


Figure 44: Behavior of controller designed for $M = 0.6$ at off-design Mach numbers of $M = 0.55$ (top), $M = 0.65$ (middle); and $M = 0.70$ (bottom).

5.4 Summary

Observers and feedback laws for suppressing oscillations in the flow past a cavity were presented using two different modeling techniques: empirical Galerkin models, and a dynamic phasor model. The Galerkin models work well for state estimation, but can be unreliable for control design, because of their very limited envelope of validity. Controllers designed from the dynamic phasor model were able to suppress oscillations completely, matching the behavior predicted by the model, as long as the control design was not too aggressive. This steady state was reached and maintained with zero average force being supplied by the actuator, only with small oscillatory forces that decrease with the amplitude of oscillations.

Of course, in experiments in which turbulence is present, one would not expect such a simple controller to be able to stabilize the flow, as this would imply removing all turbulence. However, it is reasonable to expect that a similar control design could suppress the primary resonance mechanism for cavity oscillations, and therefore significantly reduce the tones produced.

A Equations and coefficients in the two-mode shear layer model

The 2-mode model of temporal shear layer flow is

$$\dot{g} = \frac{c_{01}}{n_0} a_{1,1} a_{1,1}^* g^2 + \frac{c_{02}}{n_0} a_{1,2} a_{1,2}^* g^2 + 2 \operatorname{Re} \left(\frac{c_{03}}{n_0} a_{1,1} a_{1,2}^* \right) g^2 + \frac{1}{\operatorname{Re} n_0} \frac{d_0}{g^3}, \quad (40)$$

$$\dot{a}_{1,1} = \frac{c_{11} + g c_{12}}{n_1} a_{1,1} + \frac{c_{13} + g c_{14}}{n_1} a_{1,2} + \frac{1}{\operatorname{Re}} \left[-\left(\frac{2\pi}{L}\right)^2 + \frac{d_1}{n_1} g^2 \right] a_{1,1} + \frac{e_1}{n_1} \frac{\dot{g}}{g} a_{1,1}, \quad (41)$$

$$\dot{a}_{1,2} = \frac{c_{21} + g c_{22}}{n_2} a_{1,1} + \frac{c_{23} + g c_{24}}{n_2} a_{1,2} + \frac{1}{\operatorname{Re}} \left[-\left(\frac{2\pi}{L}\right)^2 + \frac{d_2}{n_2} g^2 \right] a_{1,2} + \frac{e_2}{n_2} \frac{\dot{g}}{g} a_{1,2}, \quad (42)$$

where the parameters are defined as follows:

$$n_0 = \int \left(y \frac{d\tilde{u}_0}{dy} \right)^2 dy \quad (43)$$

$$n_1 = \int (\hat{u}_{1,1} \hat{u}_{1,1}^* + \hat{v}_{1,1} \hat{v}_{1,1}^*) dy \quad (44)$$

$$n_2 = \int (\hat{u}_{1,2} \hat{u}_{1,2}^* + \hat{v}_{1,2} \hat{v}_{1,2}^*) dy \quad (45)$$

$$c_{01} = - \int \left(\hat{v}_{1,1} \frac{d\hat{u}_{1,1}^*}{dy} + \hat{v}_{1,1}^* \frac{d\hat{u}_{1,1}}{dy} \right) y \frac{d\tilde{u}_0}{dy} dy \quad (46)$$

$$c_{02} = - \int \left(\hat{v}_{1,2} \frac{d\hat{u}_{1,2}^*}{dy} + \hat{v}_{1,2}^* \frac{d\hat{u}_{1,2}}{dy} \right) y \frac{d\tilde{u}_0}{dy} dy \quad (47)$$

$$c_{03} = - \int \left(\hat{v}_{1,1} \frac{d\hat{u}_{1,2}^*}{dy} + \hat{v}_{1,2}^* \frac{d\hat{u}_{1,1}}{dy} \right) y \frac{d\tilde{u}_0}{dy} dy \quad (48)$$

$$c_{11} = - \int \frac{2\pi}{L} i\hat{u}_0(\hat{u}_{1,1}\hat{u}_{1,1}^* + \hat{v}_{1,1}\hat{v}_{1,1}^*)dy \quad (49)$$

$$c_{12} = - \int \hat{v}_{1,1} \frac{d\hat{u}_0}{dy} \hat{u}_{1,1}^* dy \quad (50)$$

$$c_{13} = - \int \frac{2\pi}{L} i\hat{u}_0(\hat{u}_{1,2}\hat{u}_{1,1}^* + \hat{v}_{1,2}\hat{v}_{1,1}^*)dy \quad (51)$$

$$c_{14} = - \int \hat{v}_{1,2} \frac{d\hat{u}_0}{dy} \hat{u}_{1,1}^* dy \quad (52)$$

$$c_{21} = - \int \frac{2\pi}{L} i\hat{u}_0(\hat{u}_{1,1}\hat{u}_{1,2}^* + \hat{v}_{1,1}\hat{v}_{1,2}^*)dy \quad (53)$$

$$c_{22} = - \int \hat{v}_{1,1} \frac{d\hat{u}_0}{dy} \hat{u}_{1,2}^* dy \quad (54)$$

$$c_{23} = - \int \frac{2\pi}{L} i\hat{u}_0(\hat{u}_{1,2}\hat{u}_{1,2}^* + \hat{v}_{1,2}\hat{v}_{1,2}^*)dy \quad (55)$$

$$c_{24} = - \int \hat{v}_{1,2} \frac{d\hat{u}_0}{dy} \hat{u}_{1,2}^* dy \quad (56)$$

$$d_0 = \int \frac{d^2\tilde{u}_0}{dy^2} y \frac{d\tilde{u}_0}{dy} dy \quad (57)$$

$$d_1 = \int (\frac{d^2\hat{u}_{1,1}}{dy^2} \hat{u}_{1,1}^* + \frac{d^2\hat{v}_{1,1}}{dy^2} \hat{v}_{1,1}^*) dy \quad (58)$$

$$d_2 = \int (\frac{d^2\hat{u}_{1,2}}{dy^2} \hat{u}_{1,2}^* + \frac{d^2\hat{v}_{1,2}}{dy^2} \hat{v}_{1,2}^*) dy \quad (59)$$

$$e_1 = - \int y (\frac{d\hat{u}_{1,1}}{dy} \hat{u}_{1,1}^* + \frac{d\hat{v}_{1,1}}{dy} \hat{v}_{1,1}^*) dy \quad (60)$$

$$e_2 = - \int y (\frac{d\hat{u}_{1,2}}{dy} \hat{u}_{1,2}^* + \frac{d\hat{v}_{1,2}}{dy} \hat{v}_{1,2}^*) dy \quad (61)$$

References

- [1] R. J. Adrian, B. G. Jones, M. K. Chung, Y. Hassan, C. K. Nothianandan, and A. T.-C. Tung. Approximation of turbulent conditional averages by stochastic estimation. *Phys. Fluids A*, 1(6), 1989.
- [2] J. O. Alvarez and E. J. Kerschen. Influence of wind tunnel walls on cavity acoustic resonances. 11th AIAA/CEAS Aeroacoustics Conference, AIAA Paper 2005-2804, Jan. 2005.
- [3] P. C. Bueno, Ö. H. Ünalms, N. T. Clemens, and D. S. Dolling. The effects of upstream mass injection on a mach 2 cavity flow. AIAA Paper 2004-0663, 2002.

- [4] L. Cattafesta, D. R. Williams, C. W. Rowley, and F. Alvi. Review of active control of flow-induced cavity resonance. AIAA Paper 2003-3567, AIAA Fluid Dynamics Conference, June 2003.
 - [5] L. N. Cattafesta, III, S. Garg, M. Choudhari, and F. Li. Active control of flow-induced cavity resonance. AIAA Paper 97-1804, June 1997.
 - [6] L. N. Cattafesta, III, D. Shukla, S. Garg, and J. A. Ross. Development of an adaptive weapons-bay suppression system. AIAA Paper 99-1901, May 1999.
 - [7] K. Cohen, S. Siegel, M. Luchtenburg, and T. McLaughlin. Sensor placement for closed-loop flow control of a d-shaped cylinder wake. AIAA Paper 2004-2523, June 2004.
-
- [8] T. Colonius. An overview of simulation, modeling, and active control of flow/acoustic resonance in open cavities. AIAA Paper 2001-0076, 2001.
 - [9] R. E. Dix and R. C. Bauer. Experimental and predicted acoustic amplitudes in a rectangular cavity. AIAA Paper 2000-0472, 2000.
 - [10] P. G. Drazin and W. H. Reid. *Hydrodynamic Stability*. Cambridge University Press, 1981.
 - [11] D. Fabris and D. R. Williams. Experimental measurements of cavity and shear layer response to unsteady bleed forcing. AIAA Paper 99-0605, 1999.
 - [12] J. B. Freund. Proposed inflow/outflow boundary condition for direct computation of aerodynamic sound. *AIAA J.*, 35(4):740–742, Apr. 1997.
 - [13] M. N. Glauser, H. Higuchi, J. Ausseur, and J. Pinier. Feedback control of separated flows. AIAA Paper 2004-2521, June 2004.
 - [14] J. Guckenheimer and P. J. Holmes. *Nonlinear Oscillations, Dynamical Systems, and Bifurcations of Vector Fields*, volume 42 of *Applied Mathematical Sciences*. Springer-Verlag, New York, 1983.
 - [15] Y. Guezennec. Stochastic estimation of coherent structures in turbulent boundary layers. *Phys. Fluids A*, 1(6):1054–1060, 1997.
 - [16] M. S. Howe. Edge, cavity and aperture tones at very low mach numbers. *J. Fluid Mech.*, 330:61–84, 1997.
 - [17] M. A. Kegerise. *An experimental investigation of flow-induced cavity oscillations*. PhD thesis, Syracuse University, 1999.
 - [18] H. Kook and L. Mongeau. Analysis of the periodic pressure fluctuations induced by flow over a cavity. *J. Sound Vib.*, 251(5):823–846, 2002.
 - [19] H. Kook, L. Mongeau, D. V. Brown, and S. Zorea. Analysis of the interior pressure oscillations induced by flow over vehicle openings. *Noise Control Engineering Journal*, 45(6):223–234, 1997.

- [20] K. Krishnamurty. Acoustic radiation from two-dimensional rectangular cutouts in aerodynamic surfaces. NACA TN 3487, 1955.
 - [21] O. W. McGregor and R. A. White. Drag of rectangular cavities in supersonic and transonic flow including the effects of cavity resonance. *AIAA J.*, 8(11):1959–1964, Nov. 1970.
 - [22] N. E. Murray and L. S. Ukeiley. Estimation of the flowfield from surface pressure measurements in an open cavity. *AIAA J.*, 41:969–972, 2003.
 - [23] N. E. Murray and L. S. Ukeiley. Low-dimensional estimation of cavity flow dynamics. AIAA Paper 2004-681, 2004.
-
- [24] B. Noack, K. Afanasiev, M. Morzyński, G. Tadmor, and F. Thiele. A hierarchy of low-dimensional models for the transient and post-transient cylinder wake. *J. Fluid Mech.*, 497:335–363, 2003.
 - [25] B. Noack, G. Tadmor, and M. Morzyński. Low-dimensional models for feedback flow control. part i: Empirical Galerkin models. In *2nd AIAA Flow Control Conference*, Portland, Oregon, U.S.A., June 28 – July 1, 2004. AIAA Paper 2004-2408 (invited contribution).
 - [26] B. R. Noack, P. Papas, and P. A. Monkewitz. The need for a pressure-term representation in empirical Galerkin models of incompressible shear flow. *J. Fluid Mech.*, 523:339–365, 2005.
 - [27] G. Raman, S. Raghu, and T. Bencic. Cavity resonance suppression using miniature fluidic oscillators. AIAA Paper 99-1900, 1999.
 - [28] D. Rockwell and E. Naudascher. Review—self-sustaining oscillations of flow past cavities. *J. Fluids Eng.*, 100:152–165, June 1978.
 - [29] D. Rockwell and E. Naudascher. Self-sustaining oscillations of impinging free shear layers. *Ann. Rev. Fluid Mech.*, 11:67–94, 1979.
 - [30] C. W. Rowley, T. Colonius, and A. J. Basu. On self-sustained oscillations in two-dimensional compressible flow over rectangular cavities. *J. Fluid Mech.*, 455:315–346, Mar. 2002.
 - [31] C. W. Rowley, T. Colonius, and R. M. Murray. Model reduction for compressible flows using POD and Galerkin projection. *Phys. D*, 189(1-2):115–129, Feb. 2004.
 - [32] C. W. Rowley and V. Juttijudata. Model-based control and estimation of cavity flow oscillations. In *Proceedings of the 44th IEEE Conference on Decision and Control*, Seville, Spain, Dec. 2005.
 - [33] C. W. Rowley, I. G. Kevrekidis, J. E. Marsden, and K. Lust. Reduction and reconstruction for self-similar dynamical systems. *Nonlinearity*, 16:1257–1275, Aug. 2003.

- [34] C. W. Rowley and J. E. Marsden. Reconstruction equations and the Karhunen-Loève expansion for systems with symmetry. *Phys. D*, 142:1–19, Aug. 2000.
 - [35] C. W. Rowley and D. R. Williams. Dynamics and control of high-Reynolds-number flow over open cavities. *Annual Reviews of Fluid Mechanics*, 30:251–276, Jan. 2006.
 - [36] C. W. Rowley, D. R. Williams, T. Colonius, R. M. Murray, D. G. MacMartin, and D. Fabris. Model-based control of cavity oscillations, Part II: System identification and analysis. AIAA Paper 2002-0972, 40th AIAA Aerospace Sciences Meeting, Jan. 2002.
-
- [37] C. W. Rowley, D. R. Williams, T. Colonius, R. M. Murray, and D. G. MacMynowski. Linear models for control of cavity flow oscillations. *J. Fluid Mech.*, 547:317–330, Jan. 2006.
 - [38] D. Sahoo, A. Annaswamy, N. Zhuang, and F. Alvi. Control of cavity tones in supersonic flow. AIAA Paper 2005-0793, Jan. 2005.
 - [39] M. Samimy, M. Debiasi, O. Efe, H. Ozbay, J. Myatt, and C. Camphouse. Exploring strategies for closed-loop cavity flow control. AIAA Paper 2004-0576, 2004.
 - [40] R. L. Sarno and M. E. Franke. Suppression of flow-induced pressure oscillations in cavities. *J. Aircraft*, 31(1):90–96, 1994.
 - [41] P. J. Schmid and D. S. Henningson. *Stability and Transition in Shear Flows*, volume 142 of *Applied Mathematical Sciences*. Springer-Verlag, 2001.
 - [42] R. F. Schmit, D. R. Schwartz, V. Kibens, G. Raman, and J. A. Ross. High and low frequency actuation comparison for a weapons bay cavity. AIAA Paper 2005-0795, 2005.
 - [43] L. Shaw. Active control for cavity acoustics. AIAA Paper 98-2347, 1998.
 - [44] L. Shaw and S. Northcraft. Closed loop active control for cavity acoustics. AIAA Paper 99-1902, May 1999.
 - [45] M. J. Stanek, G. Raman, V. Kibens, J. A. Ross, J. Odedra, and J. W. Peto. Control of cavity resonance through very high frequency forcing. AIAA Paper 2000-1905, June 2000.
 - [46] M. J. Stanek, G. Raman, V. Kibens, J. A. Ross, J. Odedra, and J. W. Peto. Suppression of cavity resonance using high frequency forcing—the characteristic signature of effective devices. AIAA Paper 2001-2128, May 2001.
 - [47] M. J. Stanek, G. Raman, J. A. Ross, J. Odedra, J. Peto, F. Alvi, and V. Kibens. High frequency acoustic suppression — the mystery of the rod-in-crossflow revealed. AIAA Paper 2003-0007, Jan. 2003.

- [48] G. Tadmor, B. Noack, A. Dillmann, J. Gerhard, M. Pastoor, R. King, and M. Morzyński. Control, observation and energy regulation of wake flow instabilities. In *42nd IEEE Conference on Decision and Control*, pages 2334–2339, Maui, HI, U.S.A., Dec. 2003. WeM10-4.
- [49] G. Tadmor, B. Noack, M. Morzyński, and S. Siegel. Low-dimensional models for feedback flow control. Part II: Controller design and dynamic estimation. In *2nd AIAA Flow Control Conference*, Portland, Oregon, U.S.A., June 28 – July 1, 2004. AIAA Paper 2004-2409 (invited contribution).
- [50] C. K. W. Tam and J. C. Webb. Dispersion-relation-preserving finite difference schemes for computational acoustics. *J. Comput. Phys.*, 107(2):262–281, 1993.
- [51] J. J. Thomsen. Some general effects of strong high-frequency excitation: stiffening, biasing, and smoothening. *J. Sound Vib.*, 253(4):807–831, 2002.
- [52] L. S. Ukeiley, M. K. Ponton, J. S. Seiner, and B. Jansen. Suppression of pressure loads in cavity flows. AIAA Paper 2002-0661, 2002.
- [53] L. S. Ukeiley, M. K. Ponton, J. S. Seiner, and B. Jansen. Suppression of pressure loads in resonating cavities through blowing. AIAA Paper 2003-0181, 2003.
- [54] L. S. Ukeiley, M. K. Ponton, J. S. Seiner, and B. Jansen. Suppression of pressure loads in cavity flows. *AIAA J.*, 42(1):70–79, Jan. 2004.
- [55] M. Wei and C. W. Rowley. Low-dimensional models of a temporally evolving free shear layer. AIAA Paper 2006-3228, 36th AIAA Fluid Dynamics Conference and Exhibit, June 2006.
- [56] D. R. Williams, D. Cornelius, and C. W. Rowley. Supersonic cavity response to open-loop forcing. In *Proceedings of the First Berlin Conference on Active Flow Control*, 2006.
- [57] D. R. Williams and C. W. Rowley. Recent progress in closed-loop control of cavity tones. AIAA paper 2006-0712, 44th AIAA Aerospace Sciences Meeting, Jan. 2006.
- [58] D. R. Williams, C. W. Rowley, D. Fabris, T. Colonius, and R. M. Murray. Model-based control of cavity oscillations, Part I: Experiments. AIAA Paper 2002-0971, 40th AIAA Aerospace Sciences Meeting, Jan. 2002.
- [59] K. Zhou, J. C. Doyle, and K. Glover. *Robust and Optimal Control*. Prentice-Hall, New Jersey, 1996.
- [60] N. Zhuang, F. S. Alvi, M. Alkislal, C. Shih, D. Sahoo, and A. Annaswamy. Aeroacoustic properties of supersonic cavity flows and their control. AIAA Paper 2003-3101, 2003.